Multimodal Optical Detection of Early Childhood Caries

Liang Zhang

A dissertation

submitted in partial fulfillment of the

requirements for the degree of

Doctor of Philosophy

University of Washington

2013

Reading Committee:

Eric J. Seibel, Chair

Ruikang K. Wang

Paul A. Wiggins

Joel H. Berg

Program authorized to offer degree:

Bioengineering

Contents

1 Introduction

Oral health is integral to a person's general health and is essential to their well-being and quality of life. The World Health Organization (WHO) has recognized this fact and has continued throughout the years to raise awareness in oral health as an important component of general health [51]. However, oral disease continues to be a major public health problem in developed countries, and is a growing burden in developing countries due to the adoption high-sugar and processed food diets [52, 61]. Therefore, this a global disease with few populations exempt from its effects.

Dental caries is the disease process that, if left untreated, will often progress to formation of cavities. The caries process is caused by acids produced through bacterial metabolism of carbohydrates and sugars[30]. The acids cause demineralization of the enamel surface and subsurface. If left untreated, the acid attack leads to deep structural damage of the enamel and the more porous dentin. In children, loss of teeth prematurely due caries is linked to below average weight, continued tooth decay later in life, and lower quality of life [49, 51]. As such, there is a growing need to identify at an childhood caries at an early stage, where prevention and remineralization is still possible.

Dental caries is caused by bacterial biofilms on the tooth surface, and is controlled by complex interactions between acid-producing bacteria and host factors including teeth and saliva. On exposure to oral fluids, a proteinaceous surface coating, termed the pellicle layer, is formed immediately on all solid substrates. This layer, which defines the surface charge and the nature of chemical groups exposed at the surface, changes the properties of the substrate. Bacteria colonize the surface by adhering to the pellicle through adhesion and form a biofilm, known as dental plaque. Maturation of the plaque is characterized by bacterial interactions (such as coaggregation and quorum sensing), and increasingly diverse bacterial populations. Each human host harbours different bacterial populations, including streptococci and lactobacilli bacteria, and it is thought that the metabolic interactions between different bacterial species play a key role in the maturation process of the biofilm. These bacterial species produce acids as by-products from the metabolism of fermentable carbohydrates, and cause demineralization below the surface of the tooth. The caries process is illustrated in Figure 1.

Unique amongst other mammalian calcified tissues, dental enamel is comprised approximately 80 to 90% by volume of calcium deficient hydroxyl apatite. Other calcified tissues such as bone contain significantly more organic content. However, similar to other hard tissues, enamel is hierarchical in structure with ordered features ranging micro to nano scale. On the micro scale level, enamel is highly ordered into architectural units known as enamel prisms. The developmental origin of enamel comes from the secretory product of ameloblasts, cells present
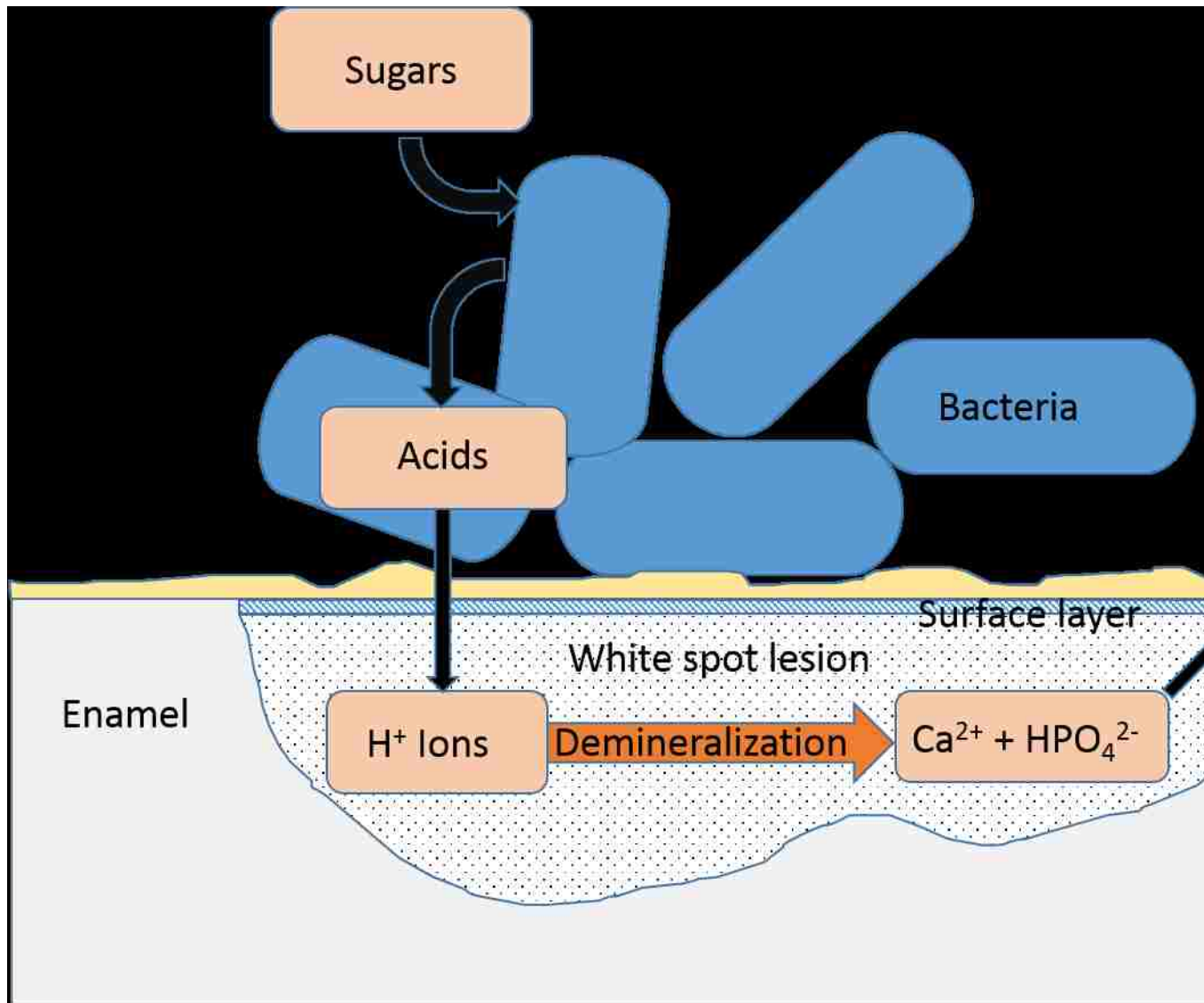
Figure 1: The caries process is caused by bacteria on the surface of the teeth metabolizing sugar and other carbohydrates to produce lactate and other acids that, in turn, dissociate to form H+ ions that demineralize the enamel beneath the surface of the tooth; calcium and phosphate are dissolved in the process. This is known as a white-spot lesion. Owing to reprecipitation, a pseudo-intact surface layer (blue stripes) is typically formed on top of the body of the carious lesion in this early stage of tooth decay.

only during tooth development, as it migrates outwardly during the process of enamel formation, known as amelogenesis. These enamel prisms are composed of highly crystalline nanorod-like calcium hydroxyl apatite crystallites that are arranged roughly parallel to one another. Typical dimensions for matured human enamel are 100 to 1000 nm in length, 26 ± 2 nm in thickness, and 68 ± 13 nm in width. The enamel rods run nearly all the way to the surface of the tooth, stopping at the final layer layer of aprismatic enamel. This prismless layer is typically 20 to 40 um thick and is thicker in deciduous teeth than in primary teeth. Looking closely at the surface of the enamel, it is possible to notice the presence of cross striations which give the apperance of ladder rungs. Similar to growth rings found in trees, these Rezius' striae incremental lines are formed due to the cyclical activity of ameloblasts, and represent hypomineralized areas. The orientation of the enamel rods and crystals within the rod and interrod enamel makes it less brittle and provides it with a certain degree of flexibility, allowing it to withstand shearing forces associated with mastication. During the caries process, acids produced from oral bacteria attack the enamel hydroxyl apatite leading to crystal dissolution (Fig. 2).

Located underneath the enamel is the dentin layer. Dentin provides support to the overlaying enamel. In contrast to enamel, the dentin is a hydrated tissue comprised of approximately, in volume, 50% mineral, 30% collagenous and non-collagenous proteins, and the remaining 20% fluids. The structure of dentin is mainly composed of type I collagen fibrils which form a three dimensional scaffold. Calcium hydroxyl apatite crystallites then form on the scaffold, reinforcing and strengthening the structure. Also unlike the enamel, dentin is a vital tissue containing the cell processes of odontoblasts and neurons. Odontoblasts perform a structural role in the formation of the dentinal matrix, and neurons convey sensory information. The primary component of the matrix, collagen, gives the tooth the resiliency necessary for the tooth to withstand the forces involved in mastication. The color of the tooth is partially due to the color as well as thickness of the dentin as well as the thinless and translucency of the overlaying enamel.

Advanced stages of demineralization can be seen on X-ray and by visual inspection performed using illumination sources such as fluorescent and incandescent lamps in combination with dental mirrors and a tactile explorer. However, X-ray and visual inspection often lacks the sensitivity to detect lesions at an early enough stage where remineralization is possible[63]. Quantitative light fluorescence (QLF) is an imaging technique to assess differences in intensities of endogenous fluorescence between demineralized and healthy enamel[64]. Although this technique has been investigated extensively in caries detection, its usefulness in detecting early stage erosions has not been established[7]. Another fluorescence technique looks for fluorescence signatures arising from byproducts of dental bacterial action. Unfortunately, bacterial fluorescence has shown to
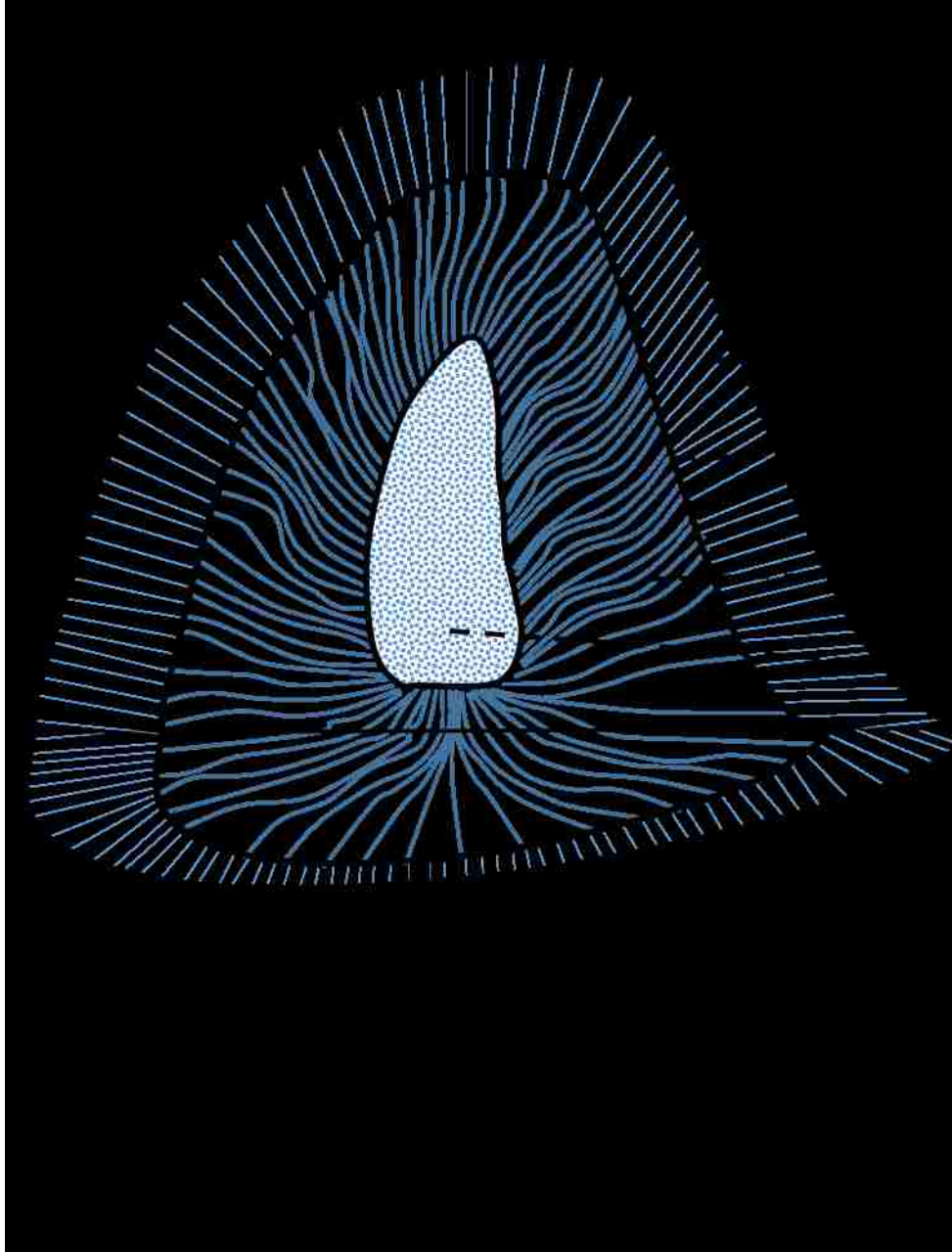
Figure 2: Diagram showing the major structures of the tooth. From the outside in, the tooth is comprised of a thin layer of aprismatic enamel, followed by prismatic enamel. The enamel-dentin junction joins the enamel with the underlying dentin. Finally, the pulp chamber is located near the center of the tooth.
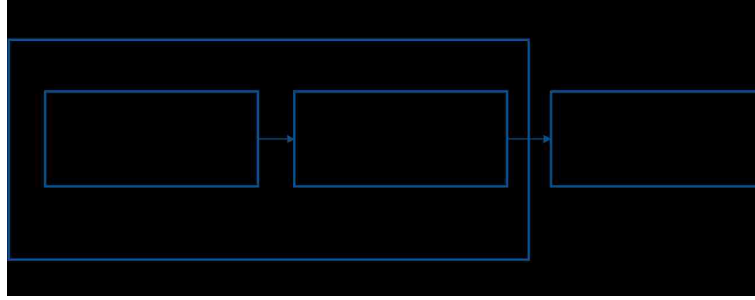
Figure 3: Overview of this research. To develop a multimodal optical device to detect early stage childhood caries, a technique for high resolution and contrast imaging of tooth surfaces is developed. This technique allows for fast survey of a tooth to locate regions of interest. Then, a diagnostic autofluorescence technique is developed to provide quantitative diagnsosis of enamel health. The different modalities are then combined together to develop a prototype clinical dental device.

be nonspecific and thus this technique has suffered in its specificity [72].

The goal of this research is to develop a multimodal optical device to detect caries at an early stage where remineralization is possible and therefore surgical intervention is not required (Fig. 3). This entails development of a technique to quickly survey for any suspicious regions on the tooth. This helps to highlight the attention of the physician to these suspicious areas. Then, a quantative diagnostic technique can be performed to diagnosis the lesion. After diagnosis, the appropriate therapeutic actions may be taken by the clinician. More specifically, this research has the following specific aims:

- Specific Aim #1: Develop an imaging modality with high resolution and high contrast for tooth surfaces.

- Specific Aim #2: Understand the mechanism for dental autofluorescence.

- Specific Aim #3: Use knowledge from Specific Aim #2 to discriminate between healthy and early stage caries.

- Specific Aim #4: Develop a clinical dental prototype for *in vivo* studies.

Development of a quick survey technique will be addressed by Specific Aim #1 and is discussed in Chapter 2. A quantative autofluorescence diagnosis technique is addressed by Specific Aims #2 and #3 and is discussed in Chapters 3 and 4. Combining both modalities into prototype clinical device as well as preliminary testing is addressed by Specific Aim #4 and is discussed in Chapters 5 and 6.

2 High Resolution and Contrast Imaging of Tooth Surfaces

2.1 Introduction

Dental caries is a complex and dynamic process, with many factors involved in the disease progression. Creating artificial dental caries that mimics the natural progression faithfully is very difficult and time consuming, and involves buffers and pH cycling. Therefore, as a first step, artificial dental erosions are used for this Aim. This gives lesions of controlled severity that are also easily reproducible.

Dental erosion is defined as the loss of dental tissue due to chemical dissolution by acids typically originating from acid beverages or gastric acid, and is steadily on the rise with highest prevalence in young children[50]. In pediatric dentistry, 6-50% of children aged 2-5 years exhibit enamel erosion[38]. The initial stages of erosion are characterized by surface enamel dissolution leading to softening of the enamel. At this early stage, natural repair of enamel by minerals in the saliva is possible. However, if left untreated, the demineralization of the enamel from the acid leads to complete removal of the enamel eventually exposing the underlying dentin. Current clinical detection of erosion is based on visual inspection, such as broad concavities within smooth surfaces of enamel, cupping of occlusal surfaces with dentin exposure, raised amalgram restorations, and loss of surface characteristics of enamel, particularly in young children[27]. By the time many of these features are clinically evident, such as dentin exposure, natural repair is no longer possible and requires surgical intervention. To address this serious pediatric health issue, various other methods have been proposed to evaluate the loss of dental enamel tissue by erosion[5].

Current techniques are generally based on observation of mineral content or surface analysis[5, 35]. Microradiography can be used to detect later stage erosion, but it is not well suited to clinical use due its ionizing nature and long exposure times[33, 11]. Optical coherence tomography (OCT) has been investigated and has potential for clinical quantification of erosion[12]. However, the cost for such devices and clinician's difficulty in interpretation of the images prevents wide scale integration of OCT technologies into the clinic. Quantitative light fluorescence (QLF) is an imaging technique to assess differences in intensities of endogenous fluorescence between demineralized and healthy enamel[64]. Although this technique has been investigated extensively in caries detection, its usefulness in detecting early stage erosions has not been established[7]. Near-infrared (NIR) imaging offers deep penetration into the dental tissue due to low enamel scattering and absorption coefficients[14, 67, 16]. On the other hand, NIR images suffer from low image resolution at long wavelengths and the bulky NIR camera systems can present a barrier for use in pediatric dental clinics [17].
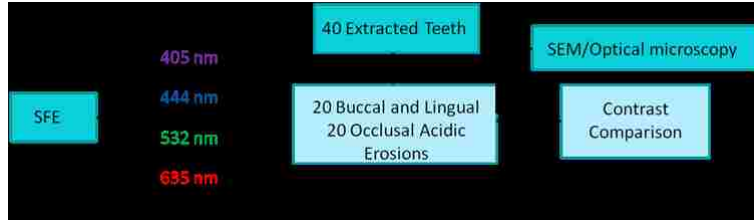
Figure 4: Flow chart of the experiment. 40 extracted teeth were used. Out of the 40 teeth, 20 teeth were used to make smooth surface erosions of varying severity and the remaining 20 were used to make occlusal surface erosions. The SFE was used to image all teeth with four different laser wavelengths. Contrast between sound and eroded enamel was then measured from the images. The artificially induced erosions were also characterized via SEM and optical microscopy.

A new laser-based ultrathin scanning fiber endoscope (SFE) technology[15] developed for cancer diagnosis[57] was used for acquiring dental images. The thin and flexible endoscope offers advantages in its multi-modal capabilities. These include RGB color, near-UV and laser-induced fluorescence (LIF) imaging. In addition, the SFE offers a threadlike form-factor that is ideal for pediatric clinical applications. The rugged mechanical construction includes a tough plastic sheath covering the Kevlar-reinforced tether. In this in chapter, we demonstrate that a short-wavelength 405 nm illumination laser using the SFE is optimal for imaging the intricate surface topography of occlusal surfaces. We also found that the 405 nm illumination laser produced good contrast images of artificial shallow erosions of less than 80um in depth located near the enamel surface. Four different laser illumination wavelengths (405 nm, 444 nm, 532 nm, and 635 nm) were evaluated in the present chapter. Reflected light images were also compared with 405 nm laser induced autofluorescence (AF) of dental enamel. Erosions of varying severity were created and erosion surface and depth were characterized by polarized transmission light microscopy, scanning electron microscopy (SEM) and dye enhanced optical microscopy.

2.2   Methods

Figure 4 is a flow chart of the experimental setup. Extracted teeth were cleaned and occlusal surfaces imaged with the SFE. From the extracted teeth, one group of smooth surface erosions and one group of occlusal surface erosions were created. The erosions were then imaged using the SFE with various laser wavelengths. The contrast was then computed between the eroded and sound enamel. Additionally, SEM and light microscopy were performed to characterize the artificial lesions. Further detail on each step is described below.

2.2.1   Specimen Preparation

The Institutional Review Board approved study used human extracted premolars and molars (n = 40). Absence of natural lesions was confirmed by using visual inspection as well as the
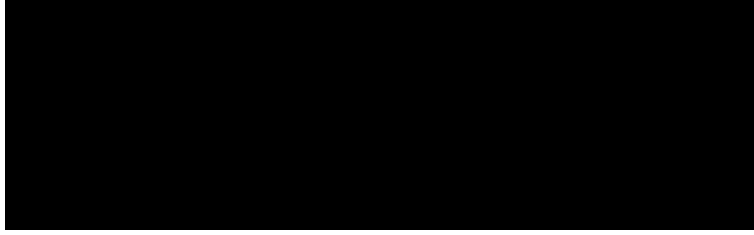
Table 1: Sample size

QLF dental diagnostic tool (Inspektor Research Systems, Netherlands)[36]. After the surfaces were gently cleaned by toothbrush and fixed using formalin (10% neutral pH formalin, Sigma-Aldrich, St. Louis, MO), the specimens were then stored in a 0.1% thymol (Sigma-Aldrich, St. Louis, MO) solution at room temperature. In preparation for inducing artificial erosions, each fixed tooth was removed from the 0.1% thymol solution and rinsed with deionized water and lightly dried with absorbing paper towelettes (Kimberly-Clark Corp., Irving, TX). Then, acid resistant varnish (Revlon Inc., New York, NY) was applied over each tooth while leaving a small window (approximately 4 x 10mm) of exposed enamel on the lingual, buccal, or occlusal side. The prepared specimens were then placed in a custom made circulating acid bath container. Twenty smooth surface and twenty occlusal surface windows were created. Prepared specimens were placed in a plastic container and submerged in an acetic acid solution of pH 3. A rotating stir bar (600 rotations per minute) was used to minimize areas of stagnant solution around the exposed enamel. Submersion times of one, two, four and six hours were used to create erosions of varying severity. After the specimens were removed from the acid solution, deionized water was used to remove and remaining acid. Then, acetone was applied onto a cotton swab, which was then used to remove the varnish. Table 1 lists the details of the specimen samples used in the chapter.

2.2.2 SFE Imaging Platform

The SFE developed in our laboratory was used to capture live video, high quality images with wide field-of-view (FOV) by actively scanning laser light instead of the conventional passive imaging from diffuse light illumination[15]. Red (635 nm), green (532 nm), blue (444 nm), or violet (405 nm) laser light can be selectively launched at the proximal end of the SFE and transmitted to the distal end using a single-mode optical fiber. The laser delivery fiber is scanned in an expanding circular pattern (up to 100 degree FOV) at the distal tip of the probe by a piezoelectric actuator, which is sealed with a lens assembly. Diffuse reflected light from the target area is collected by a concentric ring of stationary multimode fibers around the central scanning fiber. The light from the collection fibers is focused onto two color separating (dichroic)
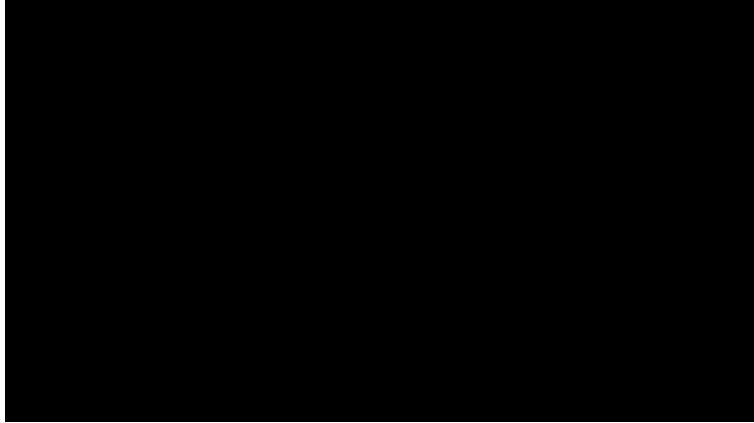
Table 2: List of key features of the SFE

beamsplitters and directed at three photomultiplier tubes (PMT). Specialized software maps the synchronized PMT signals and the instantaneous location of the spiral scanning fiber to produce a 2-D image. Specular reflections in the image are evidenced by bright spots; however by virtue of the configuration of the single, narrow beam illumination fiber and ring of collecting fibers there are relatively few spatial points meeting the specular criteria of equal angles of incidence and reflection. Hence the SFE operates without the need for crossed polarizers that reduce light collection efficiency. By utilizing this co-axial design of a single moving optical fiber with a ring of stationary collection fibers to produce 2D images, an ultrathin endoscope can be fabricated. For this chapter, a 1.2 mm diameter SFE probe was used. Table 2 summarizes the key characteristics of the SFE system. Violet and blue wavelengths were isolated by a short wavelength (460 nm) dichroic beamsplitter. The green channel consisted of light transmitted through the blue channel filter and reflected by a green (550 nm) dichroic beamsplitter. Finally, the red channel consisted of light transmitted through the green beamsplitter.16 Reflected light from the 405 nm and 444 nm illuminating lasers were collected in the blue channel and reflected 532 nm light and 405 nm AF light were collected in the green channel. The peak of 405 nm AF is centered around 480 nm[43]. Finally, 635 nm backscattered light was collected in the red channel.

2.2.3   Imaging of Surface Erosions

Wavelength dependent imaging was performed on each specimen using the SFE. The specimens were securely mounted in dental wax and the SFE probe held in a stable position using a mounting fixture so that the field of view and sample position remained constant for all images taken (Fig. 5). This procedure removed any complications from mechanical movement. Specimens were air dried for five minutes prior to imaging to emulate clinical conditions.
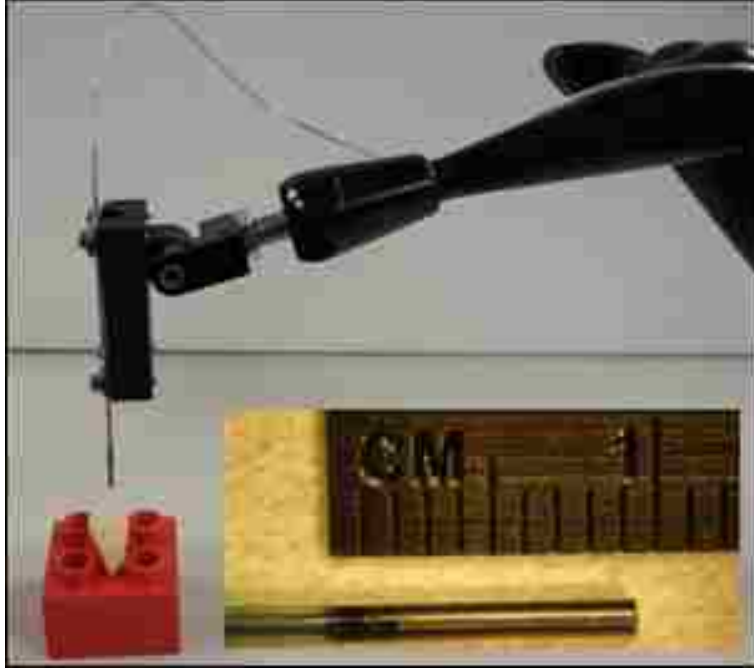
Figure 5: The SFE probe held by a mounting fixture. By scanning in an outward spiral pattern, large FOV high quality images can be obtained with a 1.2 mm diameter probe. The inset shows a magnified view of the distal end of the probe

2.2.4 Beam Spot Size Compensation/Post Processing

To rule out differences between the SFE images due to focused laser beam size, the beam diameter for 405, 444, 532, and 635 nm illumination were measured using a scanning slit optical beam profiler (BP10x VIS M2 Beam Quality Analysis System, Thorlabs, Newton, NJ). The $1/e^2$ beam diameter for each laser wavelength was recorded at a distance of 5 mm from the probe tip, which was the working distance used. For each wavelength, five measurements were recorded and averaged to improve the signal-to-noise ratio. After determining the beam diameters with the profiler, the SFE system resolution was measured with a resolution test target (Chrome-on-glass 1951 United States Air Force, Edmund Optics, Barrington, NJ). The SFE was placed 5 mm from the target in all cases. After acquiring the resolution chart images, the modulation transfer function was calculated according to MTF = (maximum intensity - minimum intensity)/(maximum intensity + minimum intensity). Intensity is the 8-bit pixel value of a slice through the test target image. To eliminate visual color bias in evaluating image resolution, all images were converted to 8-bit grayscale. Contrast and MTF were computed from these converted grayscale images. No image sharpening algorithms were used.

2.2.5 Analysis of Erosion Contrast

Analysis of erosion contrast was performed by taking a cross-section on the intensity of the image. Since images for a specimen at each wavelength were recorded at the same orientation,

the cross-section through each image represents the same physical location. To reduce noise, eleven-pixel averaging was performed on the width dimension of the cross-section line. The SFE image contrast was computed from the sound enamel and enamel containing the surface erosion according to the Weber metric:

$$W_c = \frac{I - I_b}{I_b}$$

where I is the reflected intensity of the erosion, Ib is the reflected intensity of the sound enamel, and Wc is the contrast[28]. The Weber contrast metric is often used when the image background is relatively homogenous, such as the reflections from sound enamel, and is used throughout this chapter.

2.2.6 Enamel Erosion Light Scattering

Light reflected from the tooth is a result of both surface and volume scattering. A rough surface will produce strong scattering from the front surface while a porous subsurface that contains enamel crystal fragments will result in a large contribution from scattering within the bulk[41, 42]. Isotropic (Rayleigh) backscattering will result if the pores or the crystal fragments have dimensions smaller than the illumination wavelength. To distinguish between surface and volume scattering, an enamel index matched fluid (Series B nD=1.642, Cargille Laboratories, NJ, USA), glycerol (UltraPure Glycerol, Invitrogen, NY, USA), optical gel (OC459 nD=1.6, Nye Lubricants, MA, USA), as well as a transparent viscoelastic pressure sensitive adhesive (Scotch Gloss Finish Transparent Tape, 3M, MN, USA) was applied to the front surface of the enamel to minimize diffuse reflection contributions from the erosion front surface roughness.

2.2.7 Characterizing Erosions

Healthy tooth enamel has a surface layer of aprismatic hydroxyl apatite, which is commonly referred to as the protective amorphous surface layer. During initial acid challenge, the protective surface layer is not completely removed. Rather, micro-sized pores are formed that allow acid to penetrate below the surface layer and attack the subsurface enamel, while also increasing the outer surface roughness. Additionally, the subsurface prisms are demineralized into soluble chemical species and insoluble nanoscale fragments leaving a honeycombed pattern, with areas devoid of mineral in the core of each prism[41, 42, 23, 21]. Therefore, the acid attacks both the surface layer as well as the structured hydroxyl apatite located below the surface[21]. To confirm that etched specimens follow this expected pattern of demineralization, surfaces of erosions were imaged using a scanning electron microscope (SEM) operating in secondary electron mode. For every exposure time, one tooth was selected at random to be SEM imaged. Some of the specimens

were also critical-point dried (SPI # 13200-AB Manual CPD, Structure Probe Inc., PA, USA) prior to SEM imaging. The enamel surfaces were sputter coated with gold/lead to improve electrical conductance. Examinations were carried out at 5 kV on a FEI Sirion SEM (FEI, Hillsboro, Oregon, USA). To determine erosion depth, one specimen chosen randomly for each exposure time (1 hr, 2 hr, 4 hr and 6 hr) was longitudinally fractured through the demineralized region. The fractured specimens were then submersed in a black absorbent dye (Phoenix Brands, LLC, CT, USA) overnight. Demineralized enamel become porous and thus allowed infiltration of the dye while sound enamel blocked dye penetration. After removing the specimen from the dye solution, it was then placed in epoxy (EpoxySet, Allied High Tech Products Inc., CA, USA). The fractured surface was polished starting with a 400 grit polishing disc moving up to a 1 micron diamond slurry until the surface was mostly free of scratches when viewed under a microscope. Light microscopy and erosion depth were measured on an Olympus BX51 optical microscope (Olympus Corp., PA, USA). Additionally, one specimen chosen randomly for each exposure time was used to cut 250 um sections with a microtome saw (Leica SP1600, Leica Microsystems Inc., IL USA). The sectioned erosion samples were then imaged with a polarized transmission microscope (Olympus BX51, Olympus Corp., PA, USA) to confirm the dye depth measurements[36, 66].

2.2.8   Monte Carlo Simulations

In addition to the experimental portion, a Monte Carlo (MC) model of photon transport in multi-layered tissues (MCML) [56, 47] has been adapted to light scattering in dental tissue and used in this chapter[18, 13]. The model describes the local rules of light propagation expressed as stochastic functions of the deflection in a photon's trajectory when a scattering event occurs. A modified Henyey-Greenstein phase function was applied to describe a photon's angle of deflection after each scattering event:

$$\Phi(\cos\theta) = f_d + (1 - f_d)\left[\frac{(1-g)^2}{(1+g^2-2g\cos\theta)^{3/2}}\right]$$

where fd is the fraction of isotropic scatterers, g is the scattering anisotropy, and θ is the scattering angle. When the angle of deflection is small ($\theta < 30$ degrees), scattering is mainly determined by g, while larger angles are primarily governed by fd [18, 13]. Following Fried et. al (1995) and Darling et. al (2006), fd was set to 0.35 (for 635 nm) or 0.6 (for 532 and 405 nm) for sound enamel and 0.1 (for 532 and 405 nm) for artificially demineralized enamel and μa set constant to 0.5. The input parameters for the MC simulations are listed in Table 3.

When enamel becomes demineralized, it has been reported that the scattering coefficient increases by at least a factor of ten[62, 48]. In our two layer simulation, the outermost layer
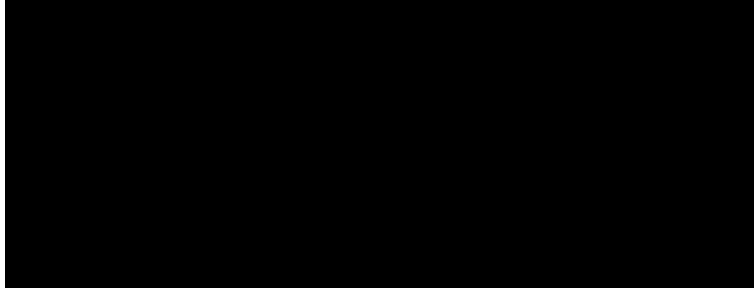
16

Table 3: Input parameters used in the MCML simulations

is immersed in air and represents demineralized enamel and thus is assigned a large scattering coefficient (μs). The layer below the demineralized zone is the sound enamel and is assigned a much smaller value of the scattering coefficient μs.The μs values for sound and demineralized enamel 1310 nm were taken from Darling et al. [13]. The μs values for sound enamel at 532 nm and 635 nm were taken directly from Fried et al. (1995)[18]. Fried et al. (1995) immersed thin enamel sections in an index matching fluid (carbon disulfide) and measured the angular dependence of light scattering. The μs for sound enamel at 405 nm was taken from experimental measurements of scattering coefficients at 405 nm by Spitzer and ten Bosh (1975)[58]. In demineralized enamel, Spitzer and ten Bosch (1977) computed experimentally the scattering coefficient changes by a factor of nearly ten from sound enamel at 340 nm, although they report standard errors of 40%[59]. It is likely that the range for increased demineralized enamel scattering at 405 nm is 5-10 times that of normal enamel scattering. The scattering coefficients used in the present simulations were 264 cm-1 for sound enamel and both 2640 cm^-1 and 1320 cm^-1 for demineralized enamel at 405 nm. The MC simulations were performed with photons directed perpendicular to the surface of the top layer. The values for dentin were taken from Fried et al. and Meng [18, 70] The refractive indices in the demineralized and sound tissue were taken to be 1.6[70].

2.3   Results

2.3.1   Image Resolution

The measured focused laser beam diameters are shown in Table 4. In agreement with the Rayleigh criterion, the focused beam size decreased as the laser wavelength decreased. However, in the case of the 405 nm laser the beam size was slightly larger than the 444 nm laser and we believe that there was some multimoding of the laser in the singlemode optical fiber, (420 nm cutoff wavelength, StockerYale, Salem, NH).

In order to compare the image quality between the violet and the red laser wavelengths, the 405 nm image was intentionally blurred using a Gaussian smoothing filter of 7 by 7 pixels,
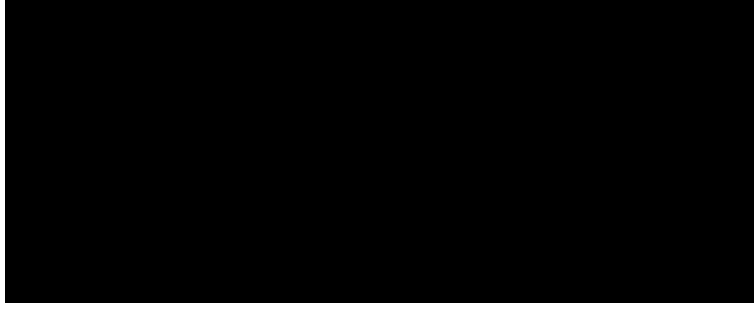
Table 4: Laser beam diameters measured 5 mm from the probe tip.

corresponding to 66 by 66 um in MATLAB (The Mathworks, Inc., MA, USA), so that the effective spot size became nearly equal between the two images. In this way, it was possible to rule out the effect of illumination spot size on the image resolution. Therefore, any differences observed between red and violet images, are attributed to the wavelength-dependent interaction between the laser and the tooth specimen. Displayed images below are spot size compensated. Shown in fig. 6 is a comparison of grayscale images taken of the occlusal surface of two extracted teeth with red (635 nm) and violet (405 nm) laser illumination. Feature details such as pitting of the walls and fissure are clearly evident in the violet illuminated image, whereas the red illuminated image is relatively blurry and such features are difficult to discern. More degrees of hypomineralization or demineralization can be seen in the 405 nm image, whereas only the gross presence of demineralization can be seen in the 635 nm image (A and C). The intricate and convoluted topography of the occlusal surface is clearly evident in the violet images (B and D).

2.3.2 Artificial Enamel Erosions

Shown in Fig. 7 is a comparison of 405 nm illumination images taken of four different teeth specimens each submerged for a different amount of time in the acid solution. Since sound enamel is a low scattering material while demineralized enamel is highly scattering, the erosion appears brighter than sound enamel in the images due to its strong backscattering [4]. It is important to note that not all teeth originated from the same patient and thus there is a possibility of inter-specimen variability in acid resistance. However, it is evident that the artificial erosion is visible for all exposure times, with overall increasing erosion/sound enamel contrast for longer submersion times.

Figure 8 shows that the 405 nm reflected images exhibited the highest contrast compared to 405 AF, red, green, and blue (635 nm, 532 nm, 444 nm) reflected images for all exposure times. At 1 hour exposure, the contrast value for the violet image was 0.3 while red, green, and blue were all below 0.1 and AF was less than 0.01. Once the exposure time was increased to 4
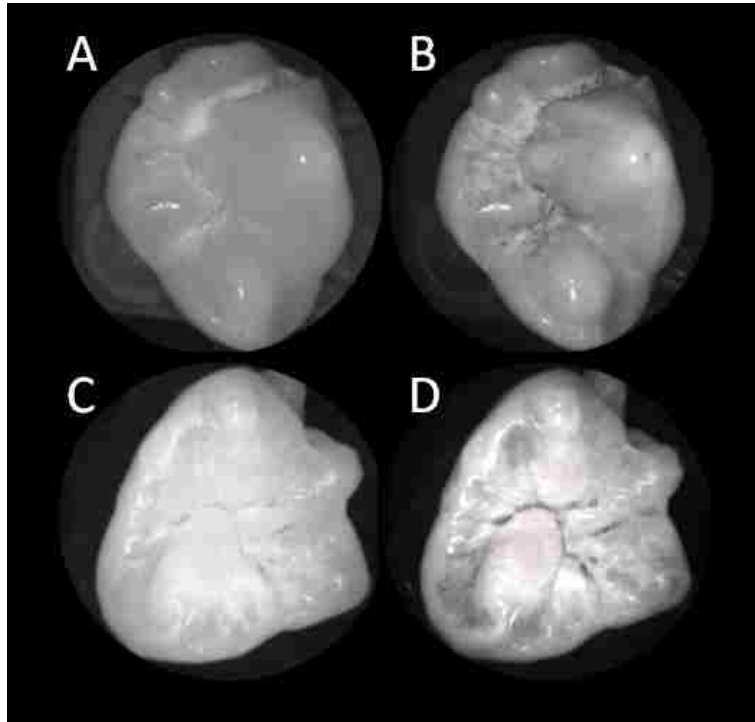
Figure 6: SFE images of the occlusal surface of a tooth illuminated with A) 635 nm and B) 405 nm lasers. SFE images of the occlusal surface of another tooth illuminated with C) 635 nm and D) 405 nm lasers. Enhanced topography details are evident in the 405 nm images. Pitting can be also seen in the violet illuminated images.

Figure 7: 405 nm reflected images of occlusal erosions produced by submersion in acetic acid solution of pH 3 for A) 6 hours, B) 4 hours, C) 2 hours, and D) 1 hour. Black arrows indicates sound enamel, while white solid arrows indicates eroded enamel.

Figure 8: Contrast between erosion and sound enamel for various illuminating wavelengths and acid exposure times. Top left: 6 hour, pH 3 exposure. Top right: 4 hour, pH 3 exposure. Bottom left: 2 hour, pH 3. Bottom right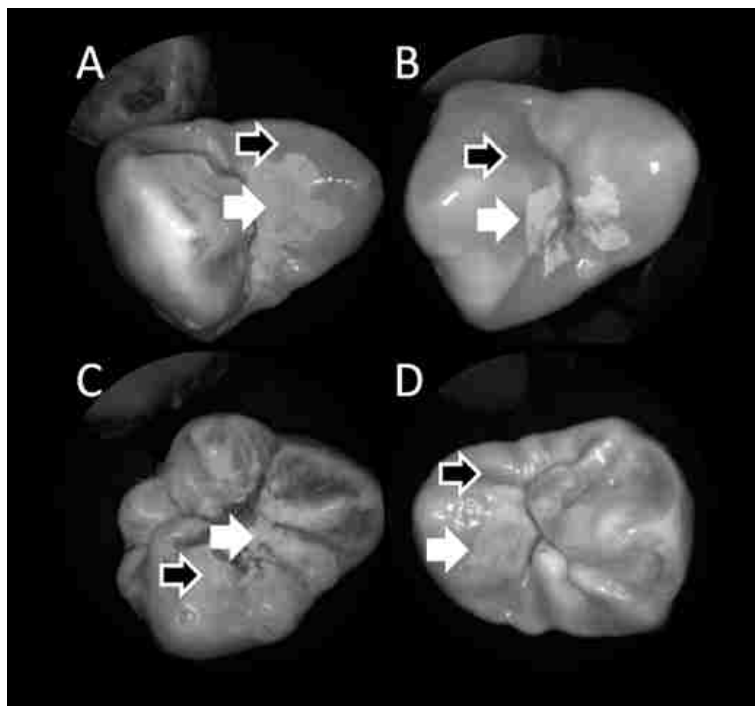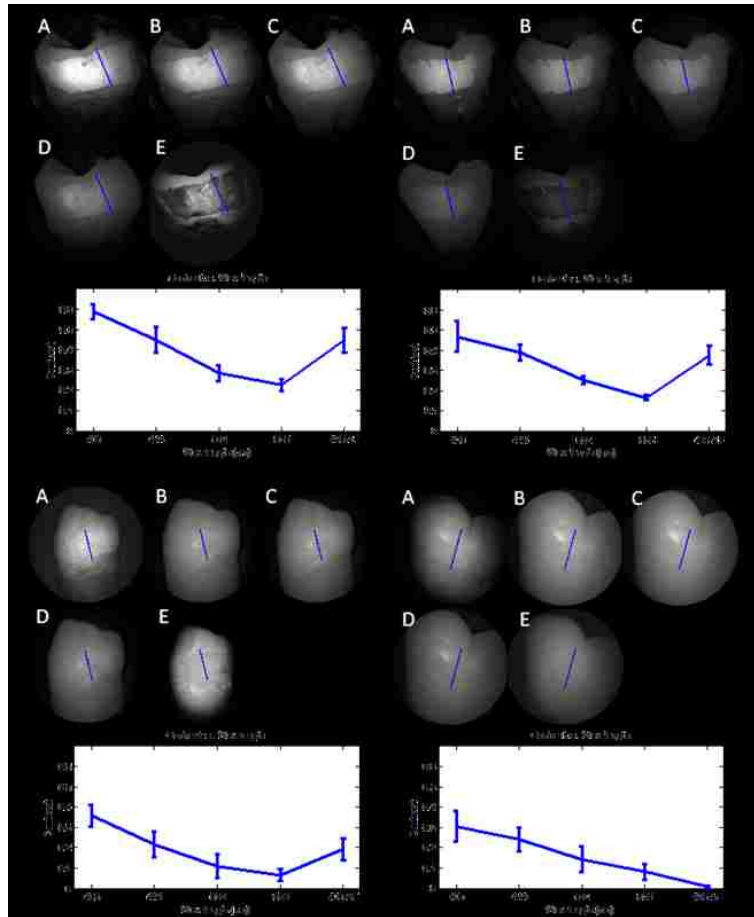: 1 hour, pH 3. For all four panes, A) 405 nm reflected image, B) 444 nm reflected image, C) 532 nm reflected image, D) 635 nm reflected image, and E) 405 nm illuminated autofluorescence image. Mean and standard deviation of measured contrast for each imaging modality are shown in the plots. Blue line in each image indicates location where contrast was measured.

or 6 hours, AF images provided the higher contrast than reg, green, and blue although violet reflected images still performed the best with a contrast value of 0.59 at 6 hours of acid exposure. Among the RGB colors, blue exhibited the highest contrast and red exhibited the lowest for all exposure times.

2.3.3 Enamel Erosion Scattering

Figure 9 shows that the 405 nm reflected images with index matched fluid and glycerol applied to the entire tooth enamel surface exhibited much lower contrast between erosion and sound enamel. In some cases, after application of the fluid, the reflected light from the erosion became lower than that of the sound enamel. This effect is seen prominently in B and D. This reversal was seen with the index matched fluid, glycerol as well as the optical gel. The time dependency for this reversal is shown in Figure 10 in the case of the optical gel. The reflected light image of the
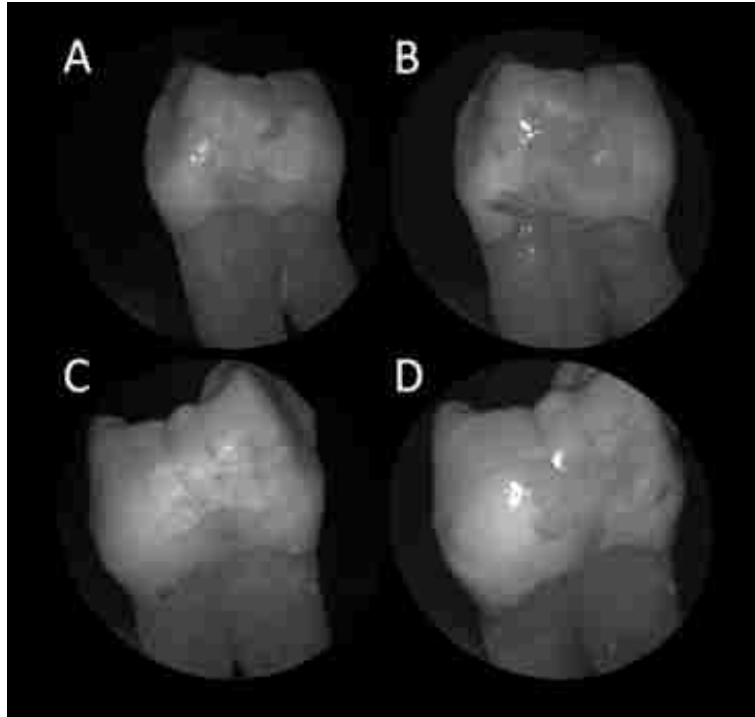
Figure 9: 405 nm backscattered image of four hour eroded specimens A) before and B) after application of index matching fluid (Top) and glycerol (Bottom). After application, a reversal in contrast is seen between the eroded and sound enamel.

eroded enamel is brighter than the surrounding sound enamel prior to application of optical gel. After application, the low viscosity gel filled up the voids in the eroded subsurface enamel over the course of two minutes. Eventually, the optical scattering of the index matched eroded enamel becomes less than that of the index matched sound enamel. However, application of a transparent viscoelastic pressure sensitive adhesive did not show this reversal of intensities, as seen in Figure 11. A small decrease in contrast was measured after application of the adhesive. The contrast value decreased from 0.6 to 0.45 for the images shown in A and B, and a reduction in contrast value from 0.42 to 0.32 was observed in C and D. Figure 12 demonstrates the effectiveness of a transparent viscoelastic pressure sensitive adhesive in wetting out the roughened surface of sandblasted glass, thus minimizing surface scattering.

2.3.4   Enamel Erosion Characterization

Surface SEM of the artificial enamel erosions show an increase in porosity in the exposed enamel as the acid exposure time was increased. The structureless surface layer in Figures 13 and 14 conceals the underlying structured enamel prisms and crystallites. However, after removal of the surface layer using critical point drying, as shown in Figure 15, demineralization of the prism cores is evident. This shows that the etched specimens used follow the expected pattern of demineralization[23, 21].
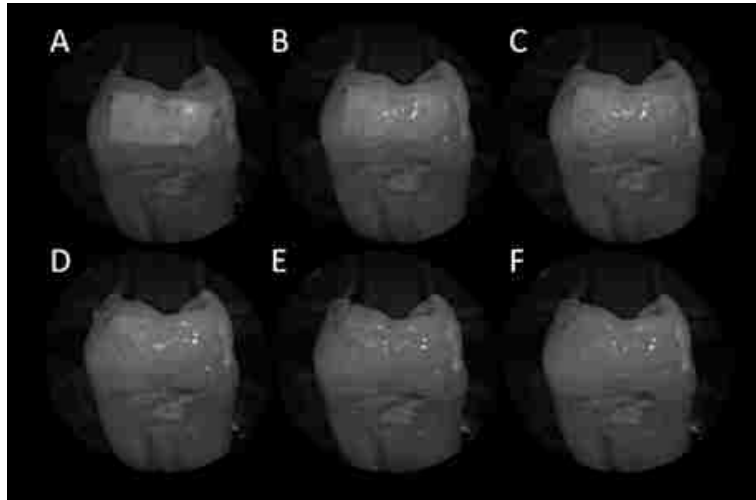
Figure 10: Time sequence of a six hour eroded specimen with application of optical gel taken at A) 0 seconds, B) 5 seconds, C) 15 seconds, D) 30 seconds, E) 1 minute, and F) 2 minutes using 405 nm illumination. A reversal of intensity between the eroded region and sound enamel occurs over this time span as the optical gel penetrates into the porous subsurface enamel within the erosion.
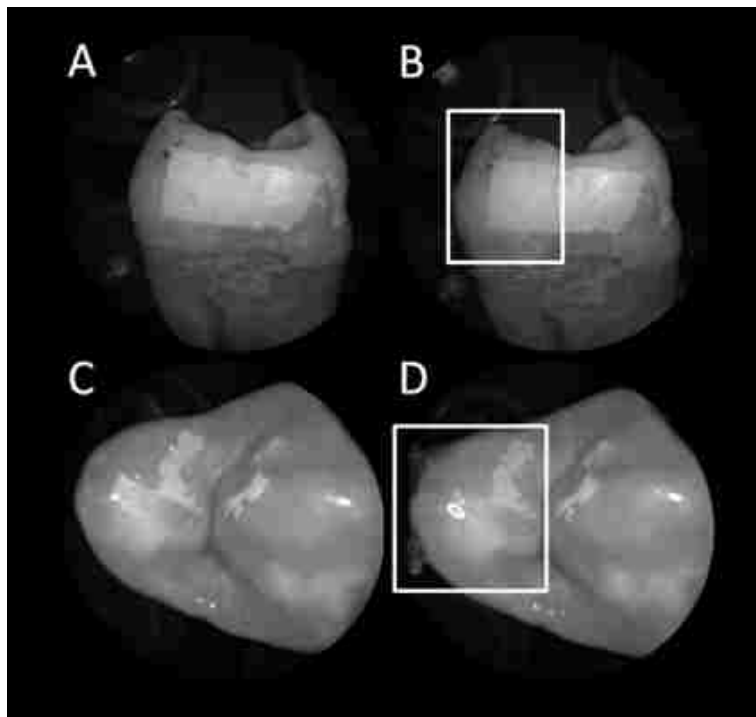
Figure 11: 405 nm images of (top) a 6 hour specimen A) prior to application of transparent viscoelastic pressure sensitive adhesive, and B) after application of adhesive. The measured contrast for this specimen is 0.6 prior and 0.45 after application of adhesive. 405 nm images of (bottom) a 4 hour occlusal specimen A) prior to application of sensitive adhesive, and B) after application of adhesive. The measured contrast for this specimen is 0.42 prior and 0.32 after application of adhesive. The white boxes in B and D represent the region where the adhesive was applied. No reversal in contrast between eroded and sound enamel is seen, indicating that the adhesive did not fill subsurface voids.
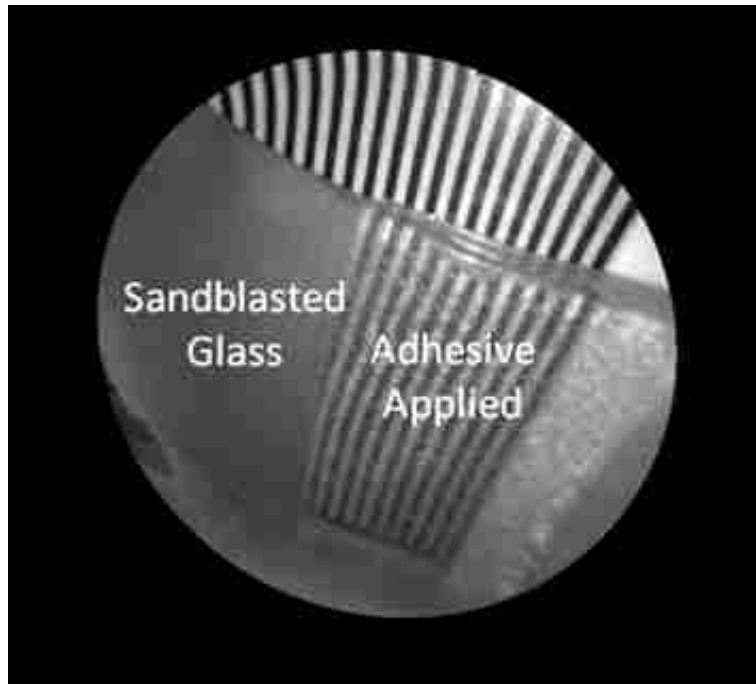
Figure 12: 405 nm image taken of sandblasted glass placed over a test target. The roughened surface scatters the 405 nm light and thus the target is not visible through the sandblasted glass. However, the textured surface was wetted out after application of the transparent viscoelastic pressure sensitive adhesive and thus the target became visible through the glass.
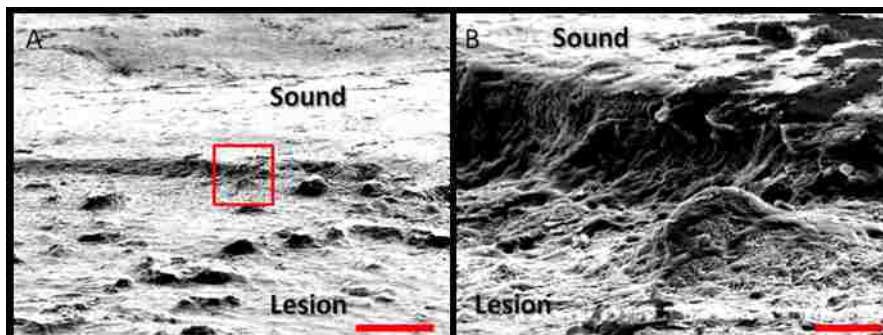
Figure 13: SEM of a specimen after acetic acid demineralization at pH 3 for 1 hour. A) bottom half of the image is the demineralized region. Scale bar is 50 μm. A zoomed in view of the red square box is shown in B. Scale bar is 5 μm. Surface of the eroded region contains pores, which are the result of the loss of mineralization.
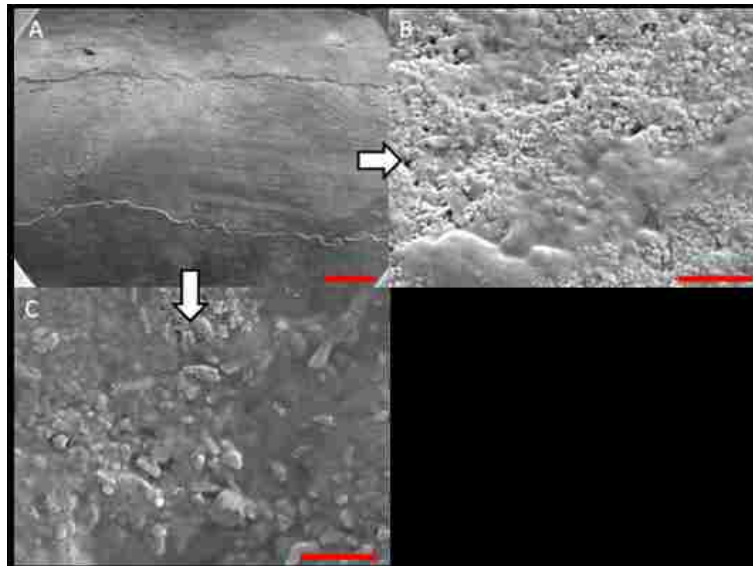
Figure 14: SEM of a specimen after acetic acid demineralization at pH 3 for 2 hours. A) Zoomed out view of erosion (center of image) and sound enamel above and below. Scale bar is 500 μm. B) Zoomed in view of center of erosion. Porous structure of the erosion is clearly evident. Scale bar is 1 μm. C) Zoomed in view of the sound enamel. Compared to the demineralized region, the sound enamel is less rough and lacks pores. Scale bar is 1 μm.
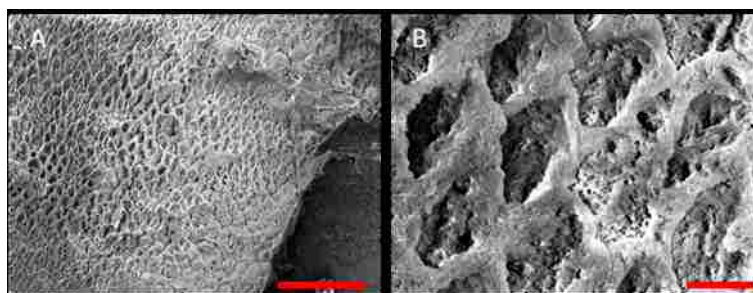
Figure 15: SEM of a tooth after acetic acid demineralization at pH 3 for 4 hours. A critical point drying technique was used to remove the surface layer without mechanical abrasion. A) Enamel prisms are seen after removal of enamel surface layer. The lower right corner of A) shows a portion of intact surface layer still present, while the central portion of the image shows the subsurface enamel. Scale bar is 50 μm. B) Zoomed in view of exposed enamel subsurface. Scale bar is 5 μm. Demineralization of the subsurface enamel is evidenced by the voids in the enamel prism cores.
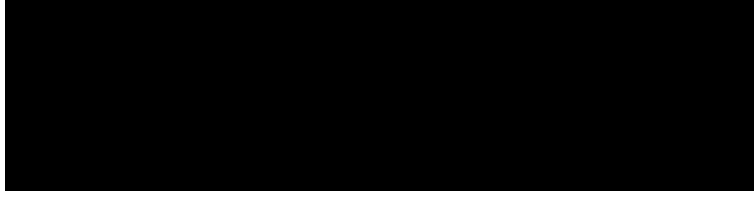
Table 5: Mean depth of erosions for various demineralization times as measured using dye enhanced microscopy and polarized microscopy
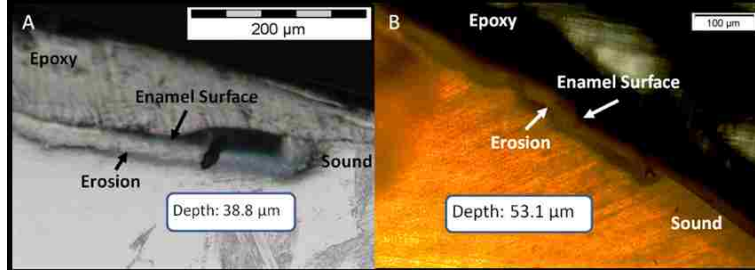
Figure 16: A) Cross section of a 4 hour eroded tooth viewed from the fractured and polished side using dye stained microscopy. Dye penetration into the demineralized channels allows for visualization of the erosion depth. The dark region to right of the arrow is a void between the epoxy and enamel. An erosion of approximately 39 μm is shown. B) Polarized transmission microscopy of a 6 hour eroded tooth from a 250 μm thickness slice. An erosion of approximately 53 μm is shown. The outer surfaces of the teeth are indicated by the arrows.

Dye enhanced microscopy yielded results similar to those of polarized transmission microscopy. Thus, the black dye staining technique allows for a relatively rapid and simple method to determine depths of artificial erosions (Fig. 16). As dye penetrated into the demineralized channels, the erosion became clearly evident. The mean depth for each erosion is shown in Table 5. As exposure times increased, erosion depth also increased. In this way, it was possible to create erosions of varying severity.

2.3.5   Monte Carlo Modeling

MC simulations were performed to model the interaction of the illuminating wavelengths with translucent enamel tissue. As stated earlier, the values of μs and f_d were taken from angular resolved scattering measurements where the enamel specimens were immersed in carbon disulfide[18]. The present work used air dried samples and therefore some differences in scattering behavior are expected. Briefly, the simulations showed that the large scattering coefficient at 405 nm yields a very shallow optical penetration depth, whereas 635 nm exhibited much deeper optical penetration. In sound enamel, Figure 17 shows that the photon flux drops by a factor of 30 at a depth of 500 μm for 405 nm illumination, while a comparable attenuation for 635 nm illumination occurs at nearly 3x the depth (1200 μm).

Artificial erosions exhibited approximately a 10x larger scattering coefficient compared to healthy enamel[13]. Therefore, 405 nm illumination will penetrate even less in demineralized
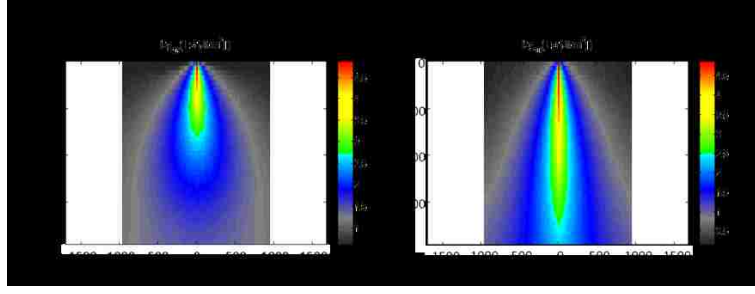
Figure 17: Flux of illuminating light into enamel tissue. Left) 405 nm photons are strongly scattered and thus do not penetrate deeply into enamel (z axis). At 500 μm, flux drops by a factor of 30. Right) 635 nm photons are not strongly scattered and therefore exhibits a high ballistic trajectory. At 1200 μm, flux drops by a factor of 30.
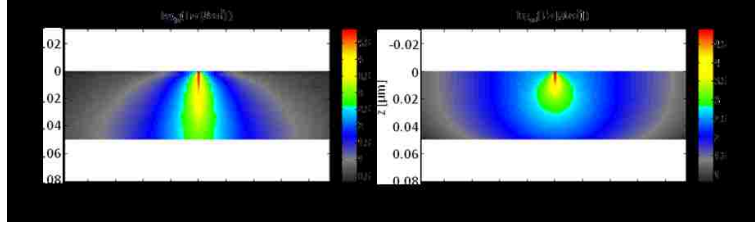
Figure 18: Photon flux for 405 nm wavelength in A) sound enamel and B) demineralized (μs = 2640 cm-1) enamel. Scattering coefficient used in A) was 264 cm-1 and in B) was 2640 cm-1.

enamel than in sound enamel. Figure 18 shows a comparison of light transport in sound and demineralized enamel. In sound enamel, the photon flux drops by a factor of 30 at a depth of 500 μm for 405 nm illumination, while a comparable attenuation for 405 nm illumination in demineralized enamel occurs at 200 μm.

Using the MC two layer model, the image contrast for demineralized enamel of increasing depths were calculated for violet and green illumination. The scattering coefficients (μs) and isotropic fractions (fd) used in the simulations are given in Table 2. The fd values for both wavelengths were taken from Fried et. al (1995) for sound enamel (fd = 0.6) at 543 nm[18]. Since the only measured value (0.1) of fd for artificially demineralized enamel was determined at 1310 nm, the same value was used in the model[13]. Figure 19 shows that the contrast between sound and demineralized enamel is higher for violet than all other simulated wavelengths. It is evident from this figure that shorter wavelengths give higher contrast than longer wavelengths.

2.4   Discussion

Because the SFE projects a beam of focused laser light and collects returned light without a focusing lens, its imaging characteristic differs from that of a conventional imaging camera. The main factors that determine the clarity of SFE enamel surface images are the penetration depth of the illumination laser into the enamel and the scattering properties within the enamel. The improved image quality observed at 405 nm compared to longer wavelengths is attributed to the
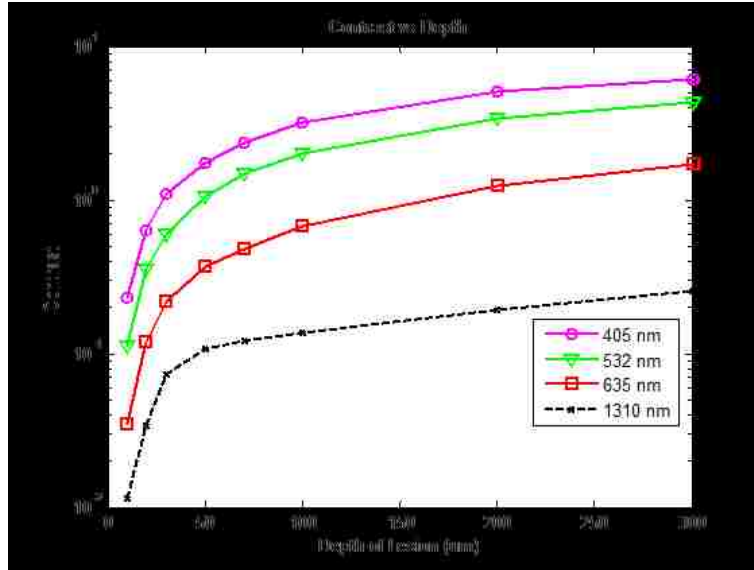
Figure 19: Demineralized enamel contrast of varying depths. MC simulations showed that illumination using 405 nm provided higher contrast than all tested wavelengths. From the simulations, shorter illuminating wavelengths provides higher contrast between sound and demineralized enamel than longer wavelengths.

relatively shallow penetration depth of the light source and concomitant reduced contribution to the collected radiation from backscattered light originating at greater depths in the enamel. The shallow penetration depth at shorter wavelength is the result of the strong wavelength dependence ($1/\lambda^3$) of the scattering coefficient[13, 39]. Hence, the reflected light collected from a short wavelength laser is not contaminated by the backscatter of light emanating from enamel tissue at greater depths. The backscattering from larger depths at longer visible wavelengths, e.g. 635 nm, is integrated and produces a composite image that diminishes the resolution of surface details.

Tooth stains have been an issue with many of the reported optical imaging techniques, although it is a lesser concern using NIR techniques[16]. Since visible light absorption is larger in the stain than in healthy enamel, interference from stains can confound autofluorescence and visible light imaging results. However, this is typically not an issue in a pediatric patient since little staining is found in children's teeth[34]. As such, the 405 nm reflected light modality applied to pediatric dentistry provides high resolution images with minor impact from stain interference in the pediatric population. As observed experimentally and confirmed by MC simulations, violet illumination exhibited the greatest contrast between sound and demineralized enamel (Fig. 19). However, the MC calculations predicted that as lesion depth increases beyond 70 microns, 405 nm contrast will plateau earlier than 532 nm illumination. This is due to the inherently large scattering coefficient and thus shallow penetration depth of 405 nm radiation. Therefore, image contrast for violet illumination plateaus when erosion depth increases beyond

the effective penetration depth of the violet light, and thus the scattering contribution from deep within the demineralized enamel is minimal. This plateau may be an issue in longitudinal studies of lesion progression, and therefore a dual wavelength contrast measurement may be necessary. On the other hand, 405 nm illumination may be ideal for early stage detection of shallow erosions, white spots, and early stage caries. The shallow penetrating 405 nm light strongly scatters in the presence of nano-sized pores and fractured demineralized enamel in the shallow subsurface, thereby increasing contrast between sound and early stage eroded enamel.

As exposure time to acid increases, surface roughness as well as demineralization depth increases[21, 3, 37]. One or both of these factors could be contributing to the increased contrast seen in the 405 nm reflection images. This problem of discriminating between surface and volume scattering cannot generally be solved by submerging samples in an index matched bath. Low to medium viscosity index matching fluids and gels are not suitable for discriminating against the contribution from surface scattering. Due to the porosity of the demineralized enamel, the index matching agent will often imbibe into the eroded enamel and thus affect both the surface and volume scattering[13]. This was observed when index matching fluid, glycerol, and optical gel were used. After application onto the tooth, the intensity of the reflection from the eroded region changed from brighter than the sound enamel region to darker than the sound enamel region over the time frame of approximately two minutes. The inversion of the contrast between the eroded and sound enamel as well as the time dependency for the inversion to occur strongly suggests that over time, the fluids eventually fill in the voids of the more porous surface enamel and also imbibe into the subsurface enamel, thus leading to lower optical scattering and therefore lower reflection intensity in the image. Thus, we were unable to separate surface from volume scattering using the liquids and gel. However, a transparent viscoelastic pressure sensitive adhesive was used successfully to separate the two optical scattering modes. The adhesive consists of a layer of weakly cross-linked polymers with a thickness of 20-100 microns[6]. The low-frequency elastic modulus of the adhesive compound, allows for deformation and can make near perfect contact with rough surfaces under low squeezing pressures[1]. The nearly complete wetting by the adhesive of the roughened outer enamel minimized surface scattering while retaining the volume scattering. Figure 20 depicts pictorially the results of acid exposure and the effectiveness of the adhesive in minimizing scattering from the surface of the roughened tooth.

We have demonstrated that short wavelength 405 nm illumination in conjunction with the SFE yields higher resolution images with enhanced surface detail compared to longer visible wavelength illumination. In addition, the reflected violet light contrast of shallow artificial erosion/sound enamel is considerably higher than for longer wavelengths. Monte Carlo simulations also confirmed the aforementioned experimental results.
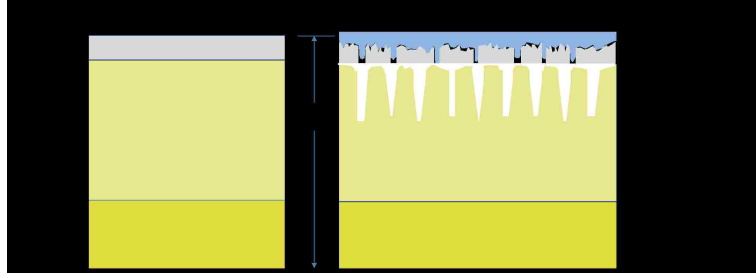
Figure 20: Cross-sectional depiction of a tooth A) prior to acid challenge and B) after acid challenge. After acid exposure, the amorphous surface layer is weakened creating a porous and roughened outer surface. The pores allow acid to attack the underlying enamel, leading to demineralized enamel prism cores. Therefore, both scattering from the surface (from the roughened amorphous layer) and subsurface volume scattering (from the porous demineralized enamel) is present. However, after the application of viscoelastic pressure sensitive adhesive to the surface of the tooth, the adhesive fills the majority of the roughened surface thus minimizing surface scattering without affecting volume scattering.

3 Nature of Dental Autofluorescence

3.1 Introduction

In the previous chapter, a high resolution and high contrast imaging modality using the SFE was developed for the purpose of rapidly surveying a tooth to spot for any suspicious. Now, there needs to be a quantative technique to diagnosis enamel health. Techniques based on auotfluorescence of the teeth have shown to be a promising technique to diagnose caries lesions. However it is currently unclear the exact governing mechanism for tooth autofluorescence. Therefore, this chapter will investigate the tooth autofluorscence and the governing mechanism behind it.

Autofluorescence is based on the presence of endogenous fluorophores residing in the enamel and dentin[40, 4]. It is well known that dental enamel and dentin exhibit laser-induced fluorescence at wavelengths longer than the excitation wavelength. Among the earliest reports of dental autofluorescence is the detection of an orange and red fluorescence of the "tooth film" in patients[9]. Later, tooth autofluorescence was observed under ultra-violet excitation[8, 31]. Since then, there have been many studies on dental autofluorescence and it has now become a diagnostic tool in caries detection (QLF, Inspektor Research Systems, Netherlands). The fluorescence spectra of sound teeth have been reported to be dependent on excitation wavelength[10]. A red shift of the excitation wavelength led to a corresponding red shift in the wavelength of maximum autofluorescence. This phenomenon will henceforth be defined as "red-shifted autofluorescence". Therefore, the governing mechanism of dental autofluorescence does not obey classical fluorescence, where the peak fluorescence wavelength is largely independent of excitation wavelength[46]. However, the mechanism governing the observed phenomenon is still unclear. Therefore, understanding the fluorescence emission mechanism of tooth enamel and dentin will be fundamental towards the development of further autofluorescence-based dental diagnostic

technologies.

In this chapter, quantitative fluorescence measurements of dental specimens were obtained. Specimens were excited at four laser wavelengths (405 nm, 444 nm, 532 nm, and 635 nm) and absolute intensity ratios were measured. These results were analyzed to determine whether Raman scattering was responsible for the red shifted spectra.

3.2   Methods

3.2.1   Specimen Preparation

The Institutional Review Board approved study used sound human extracted molars and pre-molars (n=14), ten intact specimens, two sectioned coronal dentin specimens, and two sectioned enamel specimens all with surfaces gently cleaned by toothbrush and were stored in a 0.1% thymol solution at room temperature. The dentin specimens were obtained by laterally sectioning through the center of two sound teeth. The enamel specimen was cut off the teeth and ground from the dentin-enamel junction until only enamel remained. Absence of lesions was confirmed by using visual inspection as well as the QLF dental diagnostic tool (Inspektor Research Systems, Netherlands)[36]. The surfaces of the specimens were cleaned via toothbrush, but left unpolished and curved to represent clinical situations[36].

3.2.2   Instrumentation

Emission spectra were measured using a commercial spectrometer with a grating groove density of 600 lines/mm (650 nm spectral range) and a 200 um width entrance aperture (USB 2000+, Ocean Optics Inc., Dunedin, Fla., USA). It was fitted with a 2048 element linear silicon CCD detector array (ILX511, Sony Corp., Tokyo, Japan) with a corrected linearity of greater than 99.8%. The computed resolution of the spectrometer was 4.8 nm. The experimental setup is shown schematically in Figure 21. It consists of a fiber coupled diode laser module (FTEC2, Blue Sky Research, Milpitas, CA., USA) containing a 405 nm laser diode (NDV4313, Nichia Corp., Tokushima, Japan), 444 nm fiber coupled diode laser module (FTEC2, Blue Sky Research, Milpitas, CA., USA) containing a blue laser diode (NDHB510APA, Nichia Corp., Tokushima Japan), a 532 nm fiber coupled diode laser module (FTEC2, Blue Sky Research, Milpitas, CA., USA), and a 635 nm fiber coupled diode laser module (FTEC2, Blue Sky Research, Milpitas, CA., USA). All lasers were measured with the spectrometer to confirm the laser wavelength. A 1.2 mm fiber bundle was assembled in our laboratory to guide the light from the lasers to the test specimens and deliver the autofluorescence to the spectrometer[15]. A small diameter (0.8 mm) lens, not shown in Figure 19, is positioned 150 um from the end of the laser excitation delivery fiber. The focused laser spot size at the specimen is approximately 25 um.
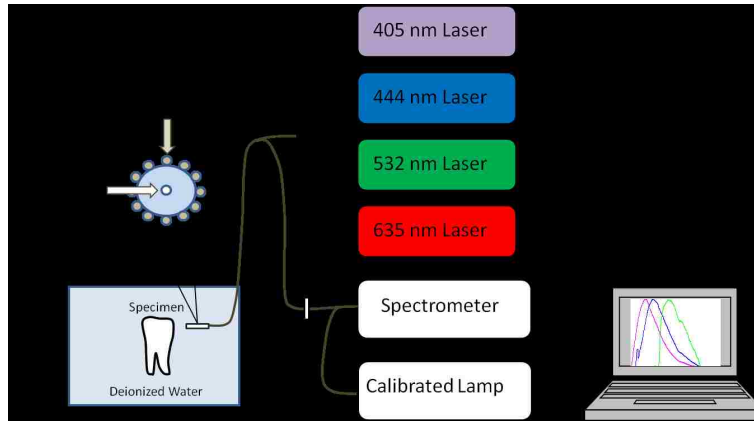
Figure 21: Schematic diagram of the experimental setup. The extracted teeth were held in a chamber filled with water. A custom flexible fiber illuminated the teeth enamel with either a 405 nm, 444nm, 532 nm, or 635 nm laser. The collected fluorescence passed through an in-line optical filter to remove laser light before entering the spectrometer. The spectra were saved on the PC and analyzed offline.

3.2.3 Procedure

Continuous wave output power was set to a constant at 1.34 mW for all lasers using an optical power meter (Model 1835-c, Newport Corp., Irvine, CA., USA). A 420 nm in-line longpass filter (E420LPv2, Chroma Technology Corp., Bellows Falls, VT., USA), or a 450 nm in-line longpass filter (NT62-982, Edmund Optics Inc., Barrington, NJ, USA), or a 532 nm in-line rejection filter (NT63-346, Edmund Optics Inc., Barrington, NJ, USA), or a 645 nm in-line longpass filter (HQ645LP, Chroma Technology Corp., Bellows Falls, VT., USA) were used individually for every excitation wavelength to attenuate excitation laser light at the spectrometer entrance aperture.

Teeth specimens were placed in a custom made chamber filled with de-ionized water. The fiber tip was placed in the chamber and submerged in the water. Fluorescence scans were performed for all four excitation lasers using a detector integration time of 100 ms. All emission spectra were recorded in a dark room to reduce stray ambient light. A universal serial bus (USB) port connected the spectrometer to a computer for spectral recordings. The spectral sensitivity of the spectrometer was corrected prior to data acquisition by a NIST-traceable (National Institute of Standards and Technology) calibrated tungsten halogen lamp (LS-1-CAL, Ocean Optics Inc., Dunedin, Fla., USA). Additionally, the dark spectrum was measured and stored, which was then subtracted out during spectral acquisition to reduce noise and further ensure removal of stray light. The spectral transmission of the fluorescence isolation filters were measured with the spectrometer and the calibrated tungsten halogen lamp.

3.2.4 Data Processing

All emission spectra were filtered with a 13-point (corresponding to a spectral width of 4.94 nm) median filter to remove electronic noise, followed by a 13-point Gaussian smoothing filter. For each sample, all emission spectra were normalized to the peak intensity of the emission spectra obtained using the 405 nm excitation laser, so that the peak intensity of the main peak of the 405 emission spectra was set to 1. By normalizing the emission spectra, we were able to compare intensity values between different excitation lasers for each tooth as well as for different teeth specimens. Additionally, another autofluorescence spectra plot was created where each spectrum was normalized to 1.0 to observe spectral shape. The measured transmission values of the fluorescence isolation filters were included into the calculations of the peak fluorescence intensity ratios. To further investigate the autofluorescence, the ratios were also determined for the two sectioned dentin specimens and two sectioned enamel specimens.

3.3 Results

All ten intact specimens exhibited autofluorescence for 405, 444, and 532 nm excitation wavelengths (fig. 22a). At 635 nm, there was no detectable autofluorescence. The emission spectra showed a broad peak centered about 50-75 nm from the excitation wavelength and gradually tapered off towards the longer wavelengths (peak fluorescence at 480 nm, 512 nm, and 579 nm for 405 nm, 444 nm, and 532 nm excitation, respectively). The shape of the spectra remained very similar regardless of the excitation wavelength (fig. 22b), except that the autofluorescence intensity diminished greatly as the excitation wavelength increased (fig. 22a). The standard deviation of the peak fluorescence signal for 512 nm and 579 nm (corresponding to 444 nm and 532 nm excitation, respectively) normalized by 480 nm (corresponding to 405 nm excitation) is shown. The small peak left of the main peak visible in the 512 nm and 579 nm spectra is from the excitation laser reaching the spectrometer that was not fully attenuated by the optical filters.

As shown in Table 6, the intensity of the fluorescence signal for an intact specimen decreased by a factor of 4.27 as the excitation wavelength increased from 405 nm to 444 nm. When the excitation wavelength changed from 444 nm to 532 nm, the ratio became 7.18. Lastly, when comparing the fluorescence intensity between 405 nm and 532 nm excitation, the intensity ratio was 30.59. It should be noted that the most sensitive ratio to examine when determining the wavelength dependence of the autofluorescence intensity is the one between the largest excitation wavelength differences, e.g. 532 nm and 405 nm (Table 6, row 3). The peak fluorescence intensity ratios for pure enamel and pure dentin are also shown in Table 6. Autofluorescence from enamel and from dentin behave similar to the autofluorescence from the ten intact teeth specimens.
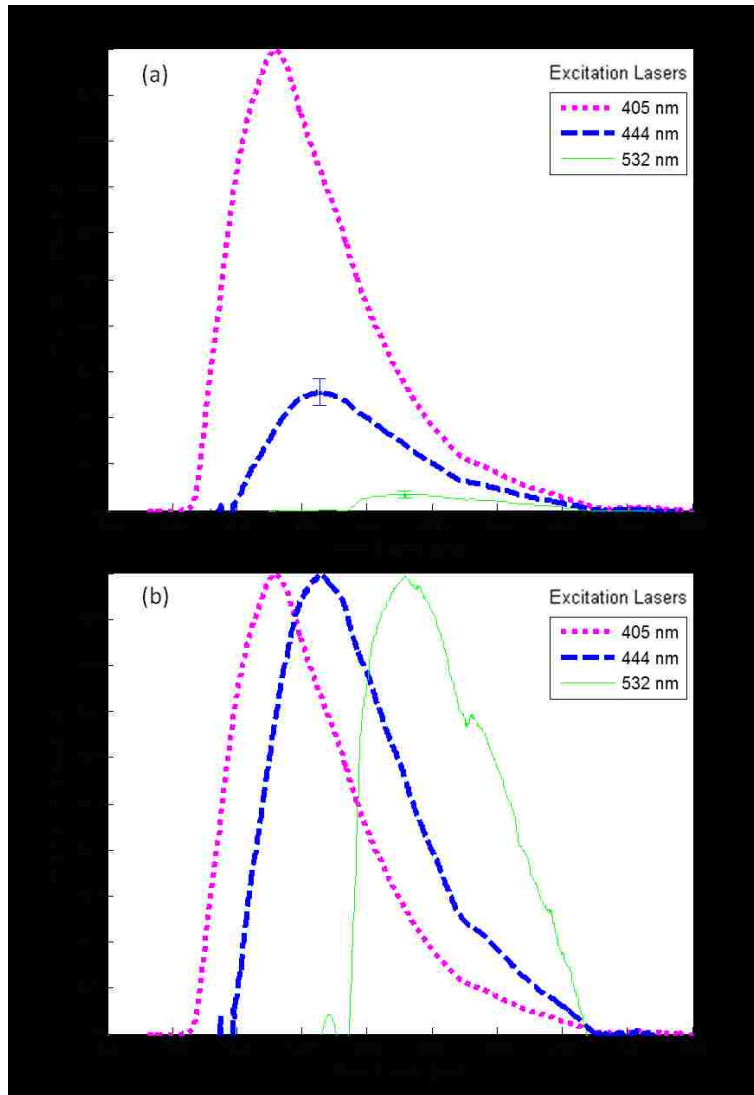
Figure 22: Averaged emission spectra for intact sound teeth (n=10) for 405 nm, 444 nm, and 532 nm excitation normalized by the peak intensity of the 405 emission spectra. (a) As excitation wavelength increased, fluorescent intensity decreased greatly. (b) Average emission spectra for each excitation wavelength normalized to their respective main peak.

Peak Fluorescence Intensity Ratio	Intact Enamel and Dentin	Enamel	Dentin	Predicted Raman Scattering
F405/F444	3.89±0.44	3.92	8.21	1.44
F444/F532	7.46±1.69	6.38	3.35	2.06
F405/F532	28.99±5.75	25.02	27.50	2.98

Table 6: Intensity ratios between the three excitation laser wavelengths.

3.3.1 Discussion

Photoexcited emission from enamel and dentin is well known and generally assigned to organic matter embedded in the inorganic calcium apatite semi-crystalline matrix.10 Buchalla has reported detailed spectra of emission from cross-sectioned enamel samples subjected to a range (380 nm to 580 nm) of excitation wavelengths[10]. He observed a red shift of the peak emission wavelength as the excitation moved to longer wavelength. In the present chapter, laser excitation of extracted teeth at three wavelengths (405 nm, 444 nm and 532 nm) revealed the same red shifted emission from sound enamel (fig. 22) as found by Buchalla. As the excitation wavelength was moved from short wavelengths (405 nm) to longer wavelengths (532 nm), the peak of the observed emission shifted from 480 nm to 579 nm, respectively.

Excitation from the ground state to an excited electronic state of a molecule generally follows the Franck-Condon Principle and favors excited and ground states with strong overlap of their vibronic levels. In many cases (e.g. non-polar fluorophore and homogeneous non-polar solvent) the excited upper electronic state rapidly relaxes to its lowest energy level on a time scale much shorter (picoseconds) than the fluorescence lifetime (nanoseconds). This non-radiative relaxation produces an emission wavelength relatively independent of the excitation wavelength. This characteristic of fluorescent light emission is often referred to as "Kasha's Rule".

Therefore, to account for the unexpected wavelength shift of the enamel emission, Buchalla mentions as a possibility that the emission from sound specimens could be due to Raman scattering rather than fluorescence. However, if the emitted wavelengths are the result of Raman scattering, their relative intensity should be proportional to the fourth power of the inverse of the exciting wavelength. Hence, the ratio of the 500 nm emission to the 560 nm emission should be $(532/405)^4$, which equals 2.97. However, this theoretical ratio is nearly 10 times smaller than the observed ratio found in this chapter (Table 6) and well outside the uncertainty range and therefore is not consistent with a Raman mechanism. In addition, a change from 405 nm to 635 nm excitation should lead to a factor of 6.04 decrease in the Raman scattering signal. However, no detectable signal was observed with 635 nm excitation. A factor of 6.04 decrease in signal should be easily detected by the spectrometer since a factor of 28.99 decrease was detected for 405 nm going to 532 nm.

Furthermore, the strong Stokes shifted Raman emission feature from the phosphate component of the dental enamel was not observed in the Buchalla spectra nor in the present chapter. The phosphate narrow band emission should appear at 960 cm^{-1} Stokes shifted from the excitation wavelength: 421 nm for 405 nm excitation and 561 nm for 532 nm excitation[24]. Lastly, the observed emission intensities are qualitatively too strong for typical Raman scattering.

Environmental factors such as fluorophore and solvent polarity can alter the conventional

pattern of fluorescent emission. The anisotropy observed in polarized fluorescence studies[?] suggests a non-uniform environment surrounding the fluorophore in the enamel and dentin, which can produce a distribution of electronic energy levels for the fluorophore. Hence a multitude of ground and excited states will exist throughout the matrix. The fluorophore in such a heterogeneous environment will behave as a collection of distinct species and thus the spectroscopic properties of this ensemble will not be uniform[26, 20].

The absorption spectra of a heterogeneously distributed fluorophore will appear broad due to the spatially nonequivalent ground and excited states. Excitation on the red-edge of the absorption band will selectively excite a specific subpopulation of fluorophores each with an electronic energy gap that matches the excitation wavelength and is a function of its local geometry. Additionally, if the timescale of obtaining a relaxed equilibrium between the fluorophore and environment is greater than the excited-state lifetime of the fluorophore, the fluorescence wavelength of these emitters will be unique to the selected sites due to its perturbed fluorophore/environment interaction (fig. 23). This phenomenon is often denoted as the "red-edge-excitation shift" (REES) or "red-edge effects" (REE)[26, 20]. Site specific excitation of a polar fluorophore at progressively increasing wavelengths on the red edge of the absorption curve will produce fluorescence at increasingly red shifted wavelengths.

A likely fluorescent component of the enamel and dentin is an amino acid based on the 3-hydroxypyridinium ring and it is the major cross-linking element of collagens[22, 60, 55]. There are two chemical forms, hydroxylysylpyridinoline (HP) and lysylpyridinoline (LP), that are based on the 3-hydroxypyridinium ring and both are naturally fluorescent. The hydroxypyridinium cross-link is present in most mature connective tissues, bone, dentin and has been recently found in enamel[68]. Collagen derives its strength from packing into cross-linked fibrils which reinforce bone, teeth and tissue. As a result, the local environment of the HP and LP fluorophores is heterogeneous in dentin and enamel since the long chain collagen is embedded in a polycrystalline calcium apatite matrix and is partially surrounded by water.

The peak absorption of both HP and LP under neutral pH conditions is located at 325 nm. Excitation at the peak absorption produces a broad (70 nm FWHM) fluorescence band centered near 400 nm. Excitation at the peak absorption wavelength leads to a large 75 nm Stokes shift that is comparable to the red shifts reported by Buchalla and observed in this study. Excitation of HP and LP at wavelengths beyond 350 nm meets the criteria for red edge excitation.

This work does not conclusively demonstrate that HP and LP are the only fluorophores. Indeed, other fluorescent species have been proposed in the past, for example tryptophan and tyrosine, and this work does not preclude their contribution to the observed fluorescence[40]. In any case, a Raman scattering mechanism does not fit the red-shifted autofluorescence.

In the work, the excitation laser was not localized to a particular depth in the whole tooth specimen. As the excitation laser wavelength increases, the depth of penetration also increases[54]. Therefore, it is expected that excitation at 635 nm and 532 nm would not only interrogate enamel but likely contain a contribution from the enamel dentin junction as well as the dentin, whereas 405 nm would be more localized to the enamel. As such, 405 nm excitation should theoretically excite less fluorophor than the longer wavelengths because it is more highly attenuated. Therefore, penetration depth cannot explain the observed dramatic decrease in autofluorescence intensity with 635 nm and 532 nm excitation (Table 6). It is known that scattering in dentin is relatively independent of wavelength[18, 19].

Therefore, if the mechanism governing the observed results is due to scattering, the spectra will not change with increasing excitation wavelengths in the dentin. The peak fluorescence intensity ratios for dentin are shown in Table 6. The autofluorescence from dentin and enamel behaved similar to autofluorescence from the ten intact specimens. In all cases, the change in peak intensity decreased by a factor of 30 going from 405 nm to 532 nm excitation, whereas only a factor of 3 decrease would be expected from a Raman mechanism. Therefore, the observed relative intensities are not strongly influenced by scattering. Laser-induced autofluorescence is a promising and exciting technology in the fight to detect early caries. Proper understanding of underlying mechanisms which govern the observed fluorescence will lead to greater insight and may permit successful detection of early carious lesions. This chapter demonstrated that dental autofluorescence intensity is heavily dependent on excitation wavelength, with an exponential decrease in emission intensity with increasing excitation wavelength, while the shape of the broad emission peak is relatively insensitive to the excitation wavelength. The governing mechanism which describes the results is provided by REES, where the heterogeneity of the fluorophore/environment population allows for different subpopulations to be excited in the red-edge of the absorption band, thus leading to an excitation wavelength dependent fluorescence spectrum.
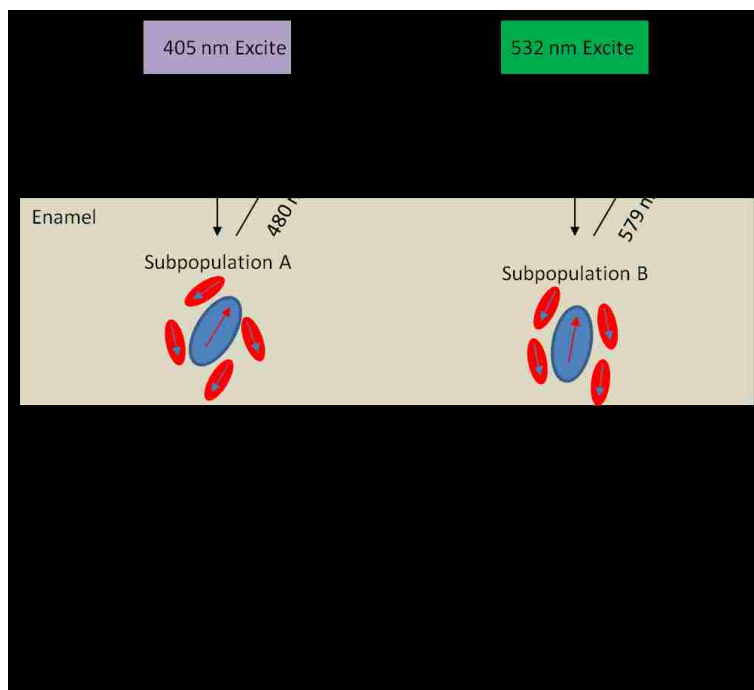
Figure 23: Pictorial representation of red-edge-excitation shift. In the enamel or dentin, a heterogeneous distribution of fluorophore (blue oval) and its calcium apatite environment (red ovals) exists. Arrows inside ovals indicate polarity. Different excitation wavelength lasers exciting on the red-edge of the absorption band of the fluorophore will selectively excite different subpopulations. In this example, 405 nm excites subpopulation A and 532 nm excites subpopulation B each with an electronic energy gap that matches the excitation wavelength. Excitation at progressively increasing wavelengths on the red edge of the absorption curve will produce fluorescence at increasingly red shifted wavelengths if the timescale of obtaining a relaxed equilibrium between the fluorophore and environment is greater than the excited-state lifetime of the fluorophore.

4 Autofluorescence to Discriminate Between Healthy and Early Stage Caries

4.1 Introduction

Dental autofluorescence (AF) is based on the presence of endogenous fluorophores residing in the enamel. It has been shown to produce excitation wavelength dependent fluorescence[10, 43]. Recently, it has been shown that dental AF behaves as a fluorophore in a rigid solvent environment, and is therefore dependent on the fluorophore/solvent microenvironment[43], as described in chapter 3. This leads to emission shifts to longer wavelengths for longer excitation wavelengths on the red-edge of the fluorophore absorption band.

The aim of this chapter was to develop a simple and robust AF ratio method to discriminate between sound enamel and different stages of early stage caries lesions. Quantitative fluorescence measurements of dental specimens were obtained using 405 nm and 532 nm laser excitation. Fluorescence from sound and early stage natural lesions were obtained and the two fluorescence spectra were analyzed. Toward this, we measured laser-induced autofluorescence spectra from sound and demineralized regions on 18 extracted human teeth. The ratio of the integrated area of the fluorescence spectra from the emission curves between 405 nm and 532 nm excitation lasers were used to develop the reference standard.

4.2 Methods

4.2.1 Specimen Preparation

The institutional approved study used extracted human molars and premolars (n = 10) with sound and early stage natural caries regions. The teeth specimens were classified using the diagnostic criteria shown in Table 7. All regions with visual signs of early stage caries were noted.

The teeth were cleaned and fixed in formalin (10% neutral pH formalin, Sigma-Aldrich, St. Louis, MO), the specimens were then stored in a 0.1% thymol (Sigma-Aldrich, St. Louis, MO) solution at room temperature. An additional (n = 8) extracted human molars and premolars were used to induce artificial erosions. To create artificial erosions, specimens with no clinically detectable natural lesions were used. Acid resistant nail varnish was applied to the enamel, leaving a window. They were then submerged in an acetic acid solution of pH 3 for four and six hours. Table 2 lists the details of the specimen samples used in the chapter.

In preparation for creating artificial erosions, each tooth was removed from the 0.1% thymol solution and rinsed with deionized water and lightly dried with absorbing paper towelettes
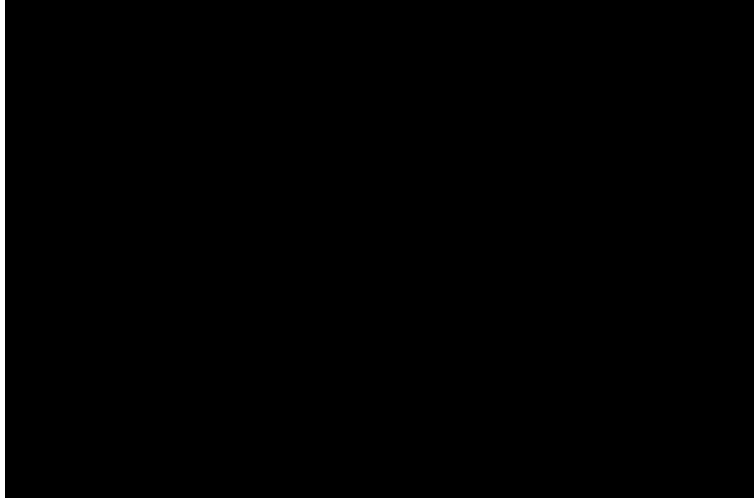
Table 7: Criteria for clinical enamel classification

(Kimberly-Clark Corp., Irving, TX). Then, acid resistant varnish (Revlon Inc., New York, NY) was applied over each tooth while leaving a small window (approximately 4 x 10mm) of exposed enamel on the lingual or buccal side. The prepared specimens were then placed in a custom made circulating acid bath container.

Eight specimens with lingual or buccal surface windows were created. Prepared specimens were placed in a plastic container and submerged in an acetic acid solution of pH 3. A rotating stir bar (600 rotations per minute) was used to minimize areas of stagnant solution around the exposed enamel. Submersion times of four (n = 4) and six hours (n = 4) were used to create erosions of varying severity. After the specimens were removed from the acid solution, deionized water was used to remove and remaining acid. Then, acetone was applied onto a cotton swab, which was then used to remove the varnish.

4.2.2 Instrumentation

A laser-induced autofluorescence spectroscopy system developed in our laboratory for early stage caries discrimination is shown in Fig. 24. The system uses a coupled diode laser module (FTEC2, Blue Sky Research, Milpitas, California) containing a 405- nm laser diode (NDV4313, Nichia Corp., Tokushima, Japan), and a 532-nm fiber coupled diode laser module (FTEC2, Blue Sky Research, Milpitas, California). Emission spectra were measured using a commercially available thermoelectrically cooled CCD array based miniature fiber optic spectrometer (QE65000 FL, Ocean Optics Inc., Dunedin, Florida). A 1.2-mm fiber bundle was assembled in our laboratory to guide the light from the lasers to the test specimens and deliver the autofluorescence to the spectrometer. A universal serial bus (USB) connected the spectrometer to a computer for spectral recording.

Continuous wave output power was set to a constant at 1.34 mW for all lasers using an optical
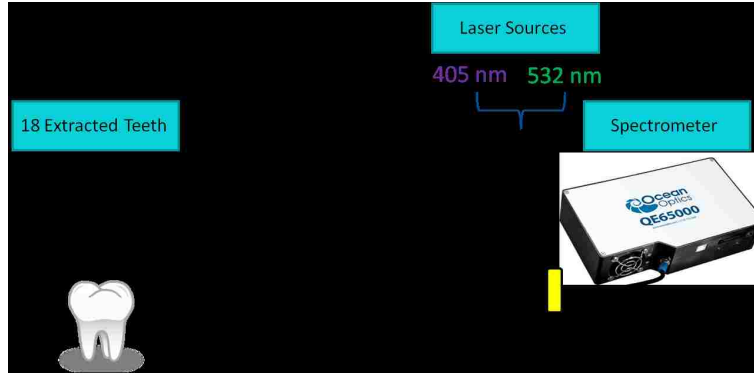
Figure 24: Schematic diagram of the experimental setup. The extracted teeth were placed in a mounting fixture. A flexible fiber illuminated the teeth with either 405 nm or 532 nm laser. The collected fluorescence passed through an in-line filter to remove the excitation laser wavelengths before entering the spectrometer. The spectra were saved on a computer and analyzed offline.

power meter (Model 1835-C, Newport Corp., Irvine, CA., USA). A 435 nm in-line longpass filter (GG 435, Schott North America Inc., Elmsford, NY, USA), and a 532 nm in-line notch filter (NF01-532U-25-D, Semrock, Rochester, NY, USA) were placed in series to attenuate both 405 nm and 532 nm excitation laser light at the spectrometer entrance aperture.

4.2.3   Data Acquisition and Processing

AF spectra excited by 405 nm and 532 nm lasers were obtained by manually alternating excitation of each individual laser on each specimen in the areas with signs of early stage caries. Additionally, AF from healthy enamel regions on each tooth was also recorded to obtain an intra-specimen standard. The spectrometer integration time was set to 100 ms to reduce system noise. Additional post filtering was then performed on the computer. All emission spectra were filtered with a 13-point (corresponding to a spectral width of 4.94 nm) median filter to further remove electronic noise, followed by a 13-point Gaussian smoothing filter.

The emitted spectra from 405 nm and 532 nm excitation were obtained from different regions on the specimens that corresponded to different stages of enamel health. The spectrum curves were integrated to obtain the area-under-the-curve. The area of the 405 nm spectrum was then divided by the area of the 532 nm spectrum to obtain the dual laser fluorescence ratio metric.

4.3   Results

All specimens exhibited AF for 405 nm and 532 nm. Fig. 25 shows a typical AF emission spectrum recorded from an early stage white spot lesion for both 405 nm excitation and 532 nm excitation. The spectra behaved in accordance with previous studies in multilaser dental fluorescence[10, 43]. The spectrum from the 405 nm excitation shows broad emission centered around 480 nm and gradually tapers off toward the longer wavelengths. The spectrum from the
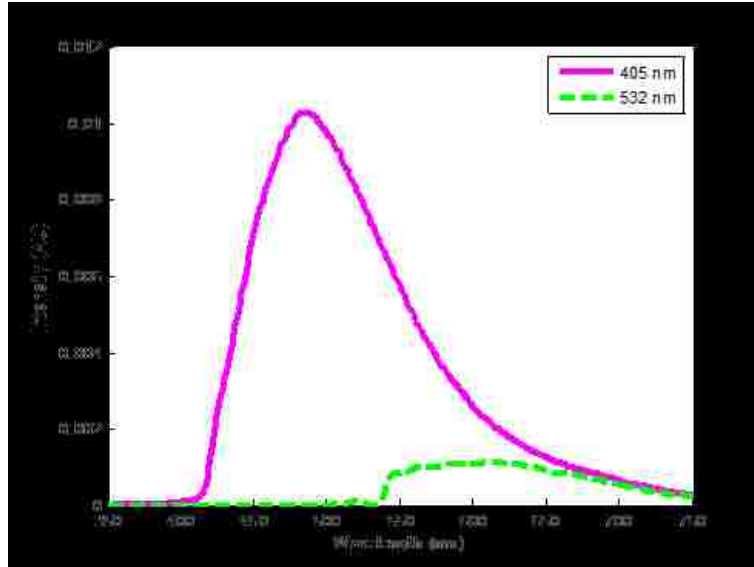
Figure 25: Typical AF spectra for 405 nm and 532 nm excitation for an early stage white spot lesion. The 405 nm spectrum centered around 480 nm and gradually tapers off in the longer wavelengths. The weaker 532 nm spectrum is centered around 580 nm and also tapers off in the longer wavelengths. In this example the dual laser ratio of area under the curve is 7.66.

532 nm excitation is similar in shape but is shifted towards red with the peak fluorescence at around 580 nm.

The 405/532 nm AF ratio is obtained from the spectra by calculating the area of both curves and dividing the 405 nm area by the 532 nm area. Fig. 26 shows the mean 405/532 nm AF ratios for healthy, eroded, early stage white spot and brown spot enamel. Healthy enamel has the highest ratio, with a trend of decreasing ratio values as severity of lesion increased. Brown spot lesions had the lowest ratio among all enamel lesions.

Table 8 shows the mean and standard error for 405/532 nm AF ratios. For each lesion classification, the ratio was computed for the lesion as well as for the healthy enamel surrounding the lesion. Percent change between the healthy and unhealthy enamel is also shown. The brown spot and early stage white spot lesions had the greatest percent change.

A series of 405/532 nm AF ratio measurements made from within a natural white spot lesion and progressing away from the lesion into the sound enamel is shown in Figure 27. An RGB image taken of the tooth from the smooth surface shows the locations of the spectral measurements (red circles). The visually difficult to perceive early stage white spot is highlighted by the blue oval. The AF ratio was low when within the white spot and progressively became larger as AF ratios were recorded from progressively healthier enamel. Almost 50 percentage change was found in this specimen between sound and caries enamel.
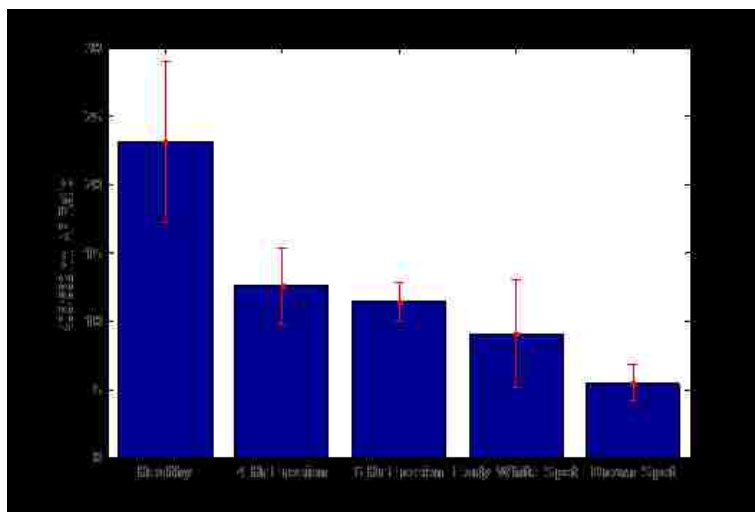
Figure 26: Mean and standard error of 405/532 nm AF ratio for healthy, 4 hour eroded enamel, 6 hour eroded enamel, early stage white spots and brown spots. Healthy enamel has the highest ratio. As enamel becomes demineralized, the ratios decreased with early white spot and brown spot lesions having the lowest ratios.
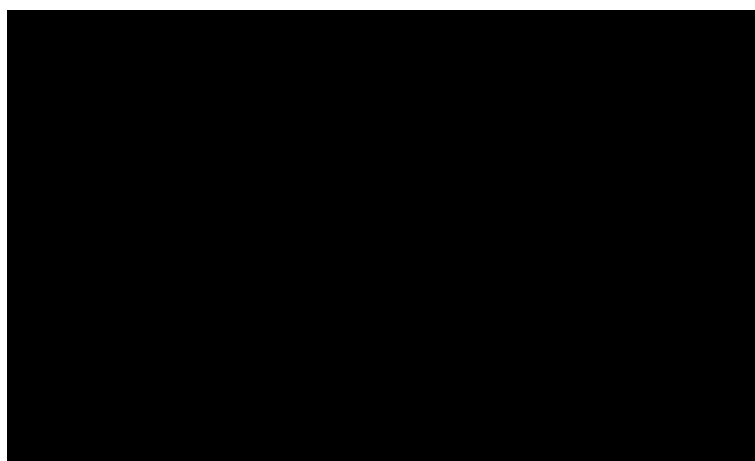
Table 8: Mean and standard error for 405/532 nm AF ratio of eroded and early stage caries lesions. Within each tooth, the mean healthy ratio and lesion ratio is used to compute the percent change.
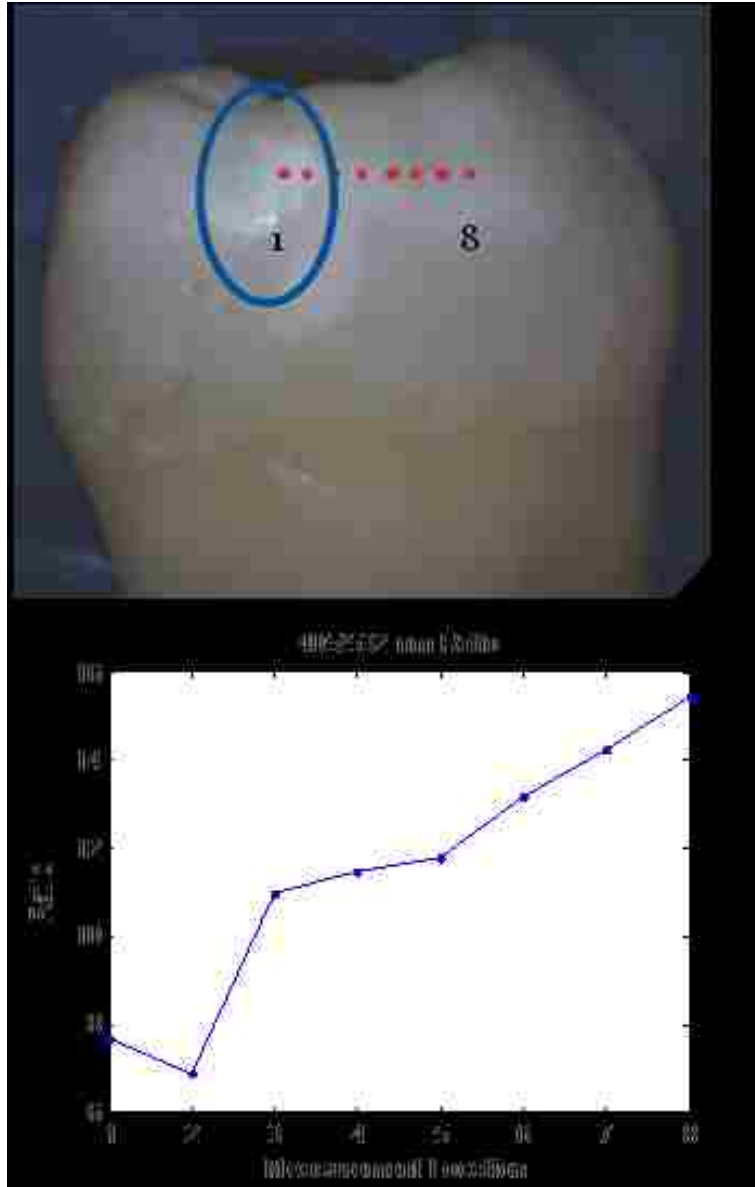
Figure 27: Series of ratio measurements made from within a natural early stage caries lesion to the surrounding sound enamel. Top) RGB image of the tooth with the early stage white spot lesion. The lesion is barely perceptible visually (blue oval). Bottom) AF ratios plotted against location on the tooth with measurement 1 inside the lesion and progressing away and into sound enamel (measurement 8). The AF ratio is low when interrogating an early stage lesion and is high when interrogating sound enamel.

4.4   Discussion

Teeth have been known to autofluoresce when excited by various laser wavelengths[10, 43, 26]. The governing mechanism for dental AF is explained well by the red-edge-excitation-shift mechanism[43]. In the enamel or dentin, a heterogeneous distribution of fluorophore and its rigid, calcium apatite matrix exists. It is proposed that the peak absorption for teeth is around 330 nm [25, 69], with collagen by-products as the most likely fluorophore[68]. Different excitation wavelength lasers exciting on the red-edge of the absorption band of the fluorophore will selectively excite different subpopulations. Thus, demineralization of the enamel due to early stage caries disrupts the normal fluorophore to matrix micro-environment. Since demineralization preferentially affects different regions in the enamel (e.g. prism cores), it is highly likely that certain subpopulations are preferentially affected and results in changes in the relative emitted fluorescence. Therefore, a change in ratios between 405 nm and 532 nm fluorescence is seen between healthy and unhealthy enamel.

Fluorescence techniques have been widely investigated for dental caries detection[63, 32, 72, 60]. However, prior techniques have attempted to detect fluorescence from bacterial byproducts or detect the absence of fluorescence due to increases in optical scattering when enamel is demineralized[72]. Bacterial fluorescence is nonspecific and absence of fluorescence is often confounded due to the geometry of the surface topography. The 405/532 nm AF technique used in this chapter detects changes in the enamel micro-environment brought upon by demineralized enamel, which is the product of early stage caries. Also, using this dual laser method allows for an internal calibration since changes in topography (due to distance from the enamel surface to the fiber tip or angle of the enamel surface with respect to the fiber will have an equal effect on both lasers. Thus, fluorescence intensity effects due to topography can be minimized when taking the ratio.

With the worldwide introduction of the sugar-rich Western diet, an alarming increase in the global prevalence of dental caries in children and adults has occurred[52]. One method to combat this impending health crisis is to detect the caries early, before permanent damage occurs. The 405/532 nm AF technique is ideal for detecting the presence of caries at an early stage, where remineralization is possible.

A low-cost benchtop or even handheld device to perform early carries detection in the developing world can be developed. Commercially available 405 nm and 532 nm lasers can now be purchased at low costs due to the commercial growth of Blu-Ray players, picoprojectors and green laser pointers. These lasers can be directly pulsed and interleaved by modulating the drive current and combined with disposable plastic transmit and return fibers to excite and collect the fluorescence emissions. Given the relatively broad emission spectra of the AF, much smaller and

lower cost microspectrometers with high dynamic range CMOS detectors with 2-10+ nm resolution (STS-VIS, Ocean Optics Inc., Dunedin, Florida) or even lower cost few wavelength spectral sensors can be used to obtain the relative intensities of the fluorescence. Laser timing and control, spectrometer I/O, radiometric calibration, and simple mathematical processes to obtain the AF ratio can all be done using simple microprocessors such as the Arduino (www.arduino.cc). The obtained ratio can be then be classified as healthy or unhealthy and then the same microcontroller can be utilized to drive LED or LCD display functions. To take a measure of early stage caries from a child, a wand can be developed that will be moved across a row of teeth, whereas an infant's few front teeth can be measured by developing a static lollipop device. In both cases, the device has cost and safety advantages compared to other means of assessing dental health, such as x-ray imaging and AF-reflectance imaging.

5   Combining Multimodal Capabilities into a Clinical Prototype

5.1   Introduction

Current clinical devices used in early dental caries detection suffer in their sensitivity and specificity [63]. Fluorescence devices that detect bacterial red fluorescence have proven to be non-specific. Additionally, devices that detect autofluorescence are very costly and bulky, and often will not work in a child's mouth. By combining the sensitive 405 nm imaging modality discussed in chapter 2 with the dual wavelength spectroscopic modality (discussed in chapters 3 and 4) that overcomes the confounding factors which plague other bacterial fluorescence devices, a multimodal imaging device can be made that utilizes the strengths of different modalities and combines them into a highly sensitive and specific device that can easily access the small and difficult to reach areas within a child's mouth.

5.2   Device Concept

The goal is to develop a clinical prototype that offers multiple modalites of operation so that the user has access to all relevant diagnostic information. The goal is to first use an imaging modality for general survey of the tooth. This modality allows the operator to rapidly survey the tooth for any regions where early caries may be suspected. After the attention has been highlighted to a region, a more quantitative diagnostic modality can be used to diagnosis the region of interest. This follows the practices of general medicine. For example, an ultrasonic investigation of arterial blood flow starts with the color Doppler modality for general imaging of blood flow. Color Doppler allows the operator to locate the vessels of interest and to see if any regions have suspicious patterns of blood flow, possibly due to plaque. After location of a suspicious region, the ultrasound machine is switched into spectral Doppler mode to quantitatively determine blood flow.

5.3   Device Design

The SFE is a highly versatile imaging device with multimodal capabilities. Using a 405 nm laser as the illuminating laser, high contrast and resolution surface imaging of tooth can be performed. This provides a general imaging modality for fast survey of a tooth. Then, by interleaving 405 nm and 532 nm laser excitation during the downtime of the spiral downtime, quantitative measurements of tooth autofluorescence ratios may be obtained for diagnosis of enamel health.
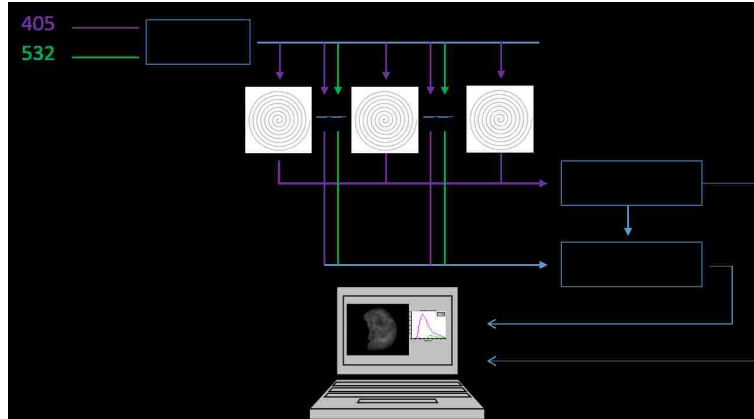
Figure 28: Flow diagram for the early caries detection clinical prototype. A fiber switcher will control which illumination source is used (either 405 nm or 532 nm). During the spiraling scan pattern of the SFE, 405 nm will be used to obtain the high contrast and resolution surface imaging of the tooth surface. Then, when the user wishes to capture spectroscopy, the user will push a software button and the scanning fiber will temporarily halt. During the scanning deadtime, the excitation laser source will be alternated between 405 nm and 532 nm. The emitted fluorescence from the tooth will be collected by the return fibers on the SFE probe and transmitted to an attached spectrometer. The spectra will be collected and transmitted to a PC via a universal serial bus where the ratio can be computed and displayed

5.3.1 Protoype Flow Chart

Shown in Figure 28 is a flow chart for the prototype clincal device. Two lasers will be used, 405 nm and 532 nm. They will be passed into a fiber switcher which can be controlled to output either lasers. The SFE will operate as usual. During the spiral scan step, the SFE will be performing its imaging using 405 nm as its illumination laser. Then, when the user wishes to capture spectroscopy, the user will push a software button and the scanning fiber will temporarily halt. During the scanning fiber's deadtime (when the resonant fiber is not scanning), the fiber switcher will be controlled to alternate between 405 nm and 532 nm as it's output. The emitted fluorescence can then be collected by an attached spectrometer. This then allows for acquisition of point autofluorescence spectra with both lasers, therefore obtaining the autofluorescence ratio.

The SFE probe configuration will be slightly modified so that collected light can be delivered to both the SFE and the spectrometer. To do so, a bundle of optical fibers will be attached parallel to the SFE probe. The distal end of the bundle will collect returned fluorescence light and transmit it to the proximal end where it is attached to the spectrometer. This way, the SFE probe itself needs not be altered and will continue outputing and scanning the laser as well as returning reflected light into the SFE to perform the 405 nm imaging.

5.3.2 Spectrometer Control

Since there will always be signal (reflected and autofluorescent light) being transmitted into the spectrometer, there needs to be way to control the spectrometer so that it only records

spectra during the down time between SFE spiral scans. The spectrometer that will be used is an Ocean Optics QE 6500FL spectrometer. The spectrometer can be controlled using C++, Java, or LabView using Ocean Optics' provided library files. For example, the spectrometer is easily controlled using the provided Wrapper class in Java. Figure 29 provides a simple program obtain a spectrum from the spectrometer. More specifically, it:

- Opens all attached spectrometers to the PC

- Obtains the basic information about the spectrometer such as its name and serial number

- Sets the spectrometer integration time to the minimum integration time

- Checks to see if the spectrometer has a thermo-electric cooling feature. If it does, then it cools the spectrometer

- Obtains one spectrum from the spectrometer and then outputs the spectrum in console
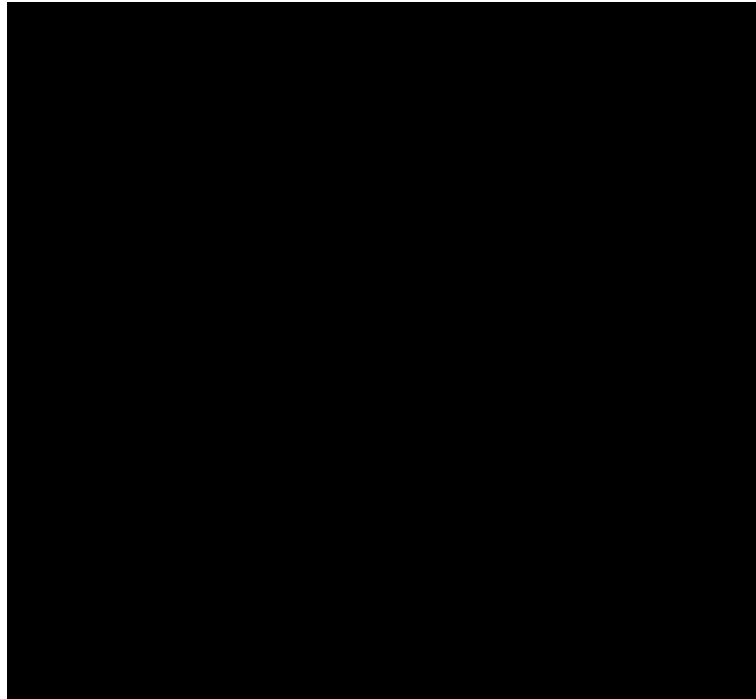
5.3.3 Components

The primary components needed for the assembly of the clinical prototype device are the SFE and its probe, and the spectrometer. However, many other smaller components are also needed. Below is a list of the necessary components for the assembly of the device:

- Scanning Fiber Endoscope
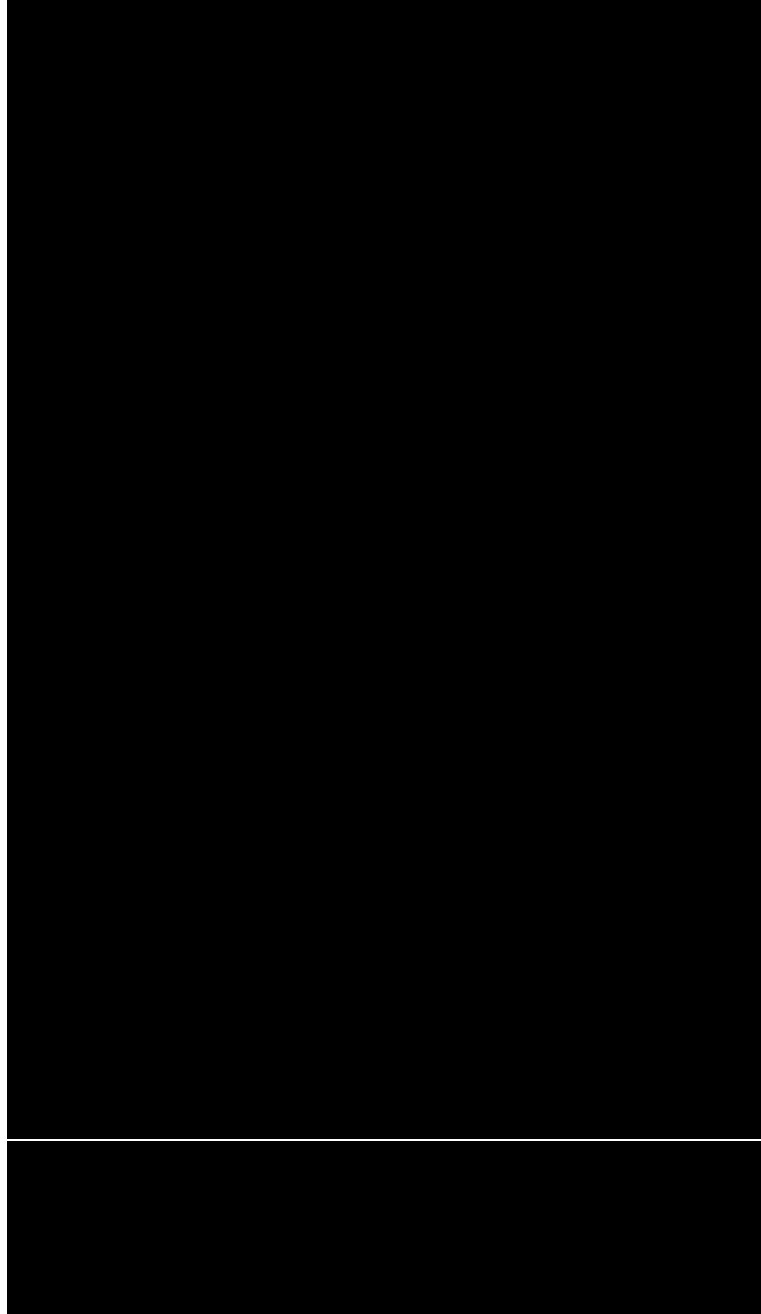
- 405 nm laser- FTEC2, Blue Sky Research

Figure 29: Example Java code to obtain a spectrum from the spectrometer

- 532 nm laser- FTEC2, Blue Sky Research

- Fiber Switcher- SN series, Sercalo Microtechnology

- Optical Fibers- 405 hp, Nufern

- Spectrometer- QE65000FL, Ocean Optics

- Fluorescence filters- GG 435, Schott, NF01-532u, Semrock

- Computer- Sony Vaio PCG-61315L with Eclipse Java Development Environment and Lab-view 10

In addition to these components, Institutional Review Board approval has already been approved so that *in vivo* testing may be performed.

6 Clinical Device Development and Testing

6.1 Introduction

In this chapter, we describe the development and initial testing of the multimodal clinical prototype device. The device allows the user to quickly and easily screen all teeth by first imaging using 405-nm reflectance, autofluorescence (AF), and bacterial fluorescence. Once a suspicious region in a tooth is identified, the user can temporarily halt the imaging to obtain detailed fluorescence spectroscopic data. The obtained spectra are analyzed and an AF ratio is computed, which can be used to quantitatively diagnose enamel health.

The development of the device and initial testing is described below. Extracted teeth with clinically diagnosed carious lesions were examined using the device. Histology was also performed on the examined teeth using polarized light microscopy (PLM). To test the operating capabilities of the clinical prototype device in a clinical patient setting, the device is also tested on five patients in vivo, with one case reported for a detailed description.

6.2 Methods

The multimodal device is a clinical prototype that is capable of capturing and displaying, in real time, three imaging modes. These modalities are short-wavelength laser reflectance images, autofluorescence and bacterial fluorescence images. Additionally, the device is capable of capturing autofluorescence spectra to compute a metric which may be used to determine enamel health. The device and its different modules are first presented. Then, the use of the device on both extracted and in vivo teeth is described. Histology was performed to validate findings.
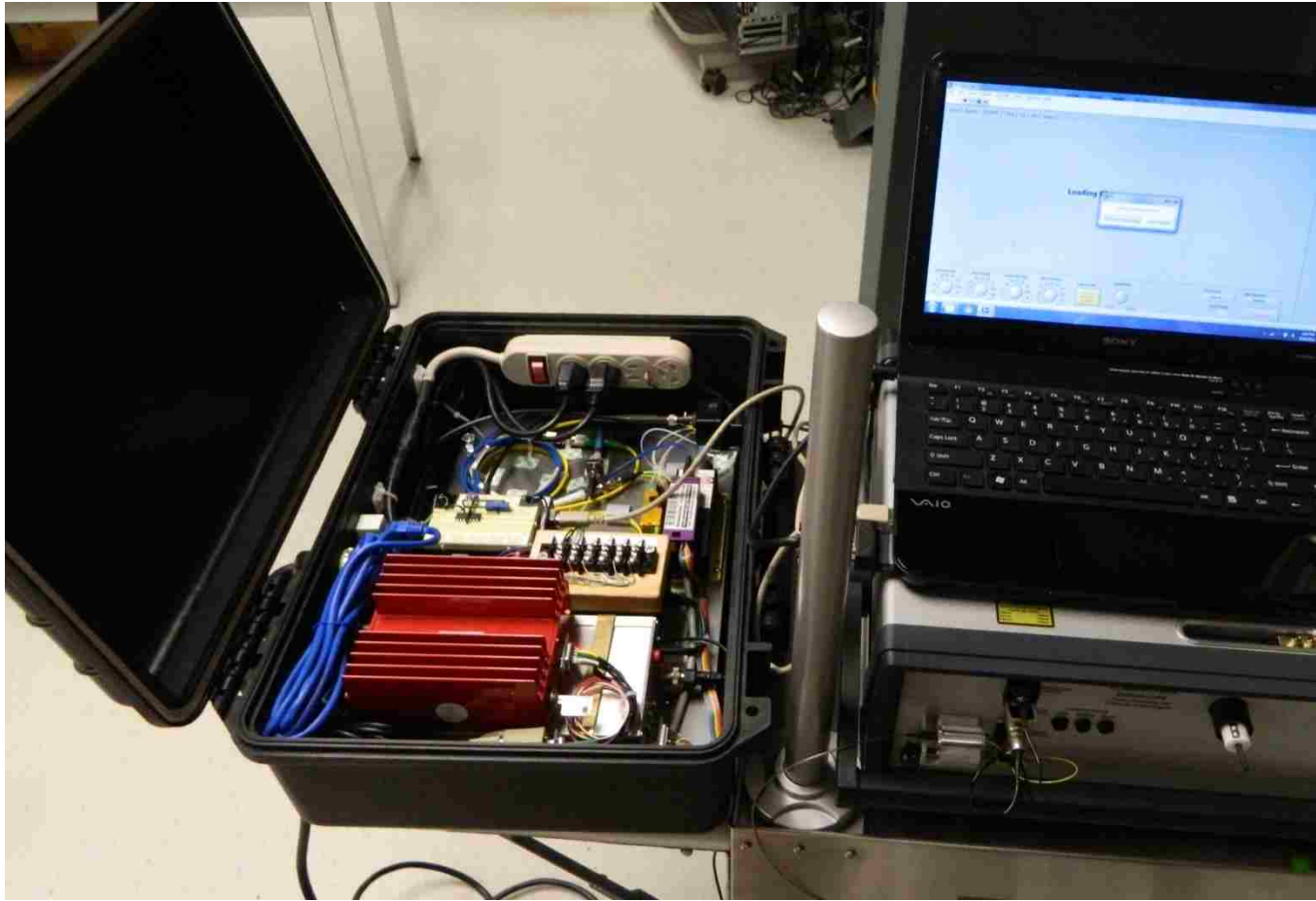
Figure 30: The multimodal caries detection clinical prototype device. The scanning fiber endoscope imaging module in the photo is beneath the laptop computer. Live video images are sent in real-time to a display monitor (not shown). The spectrometer module which also houses the two lasers is packaged into a mobile case. The spectrometer case is open in the photo but may be closed during clinical examinations.

6.2.1 Device Design

The clinical prototype device is an optical device capable of different modes of operation (Fig. 30). These modes include 405 nm reflectance imaging, 405 nm induced autofluorescence imaging, bacteria fluorescence imaging, and dual laser fluorescence spectroscopy. These modes of operation can be performed separately or simultaneously.

The multimodal optical device for early caries detection can be separated into two major functions, imaging and spectroscopy. For the real-time imaging of the teeth, the device utilizes the scanning fiber endoscope (SFE) engine. For dual laser spectroscopy, the device utilizes a fiber-optic coupled miniature spectrometer. A detailed description of the device is presented below.

Imaging Modality	Clinical Use
405 nm Reflectance	High resolution and high contrast surface imaging for initial surveillance
405 nm induced Autofluorescence	Confirmation/screening for potential caries lesions
405 nm induced bacterial Fluorescence	Presence of plaque/bacterial activity

Table 9: Different imaging modalities and their use

6.2.2 Imaging Modality

The SFE developed in our laboratory is a miniature fiber endoscope that can be used to capture live video, high-quality images with wide field-of-view by active scanning of a laser light beam instead of the conventional passive imaging method using diffuse light illumination [15]. The laser beam is scanned in an expanding circular pattern (up to 100 degree FOV) at the distal tip of the probe by a piezoelectric actuator, which is sealed with a lens assembly. Diffuse reflected light from the target area is collected by a concentric ring of stationary multimode fibers around the central laser beam scanning fiber. The light from the collection fibers is focused onto two color separating (dichroic) beamsplitters and directed at three photomultiplier tubes (PMT). Specialized software maps the synchronized PMT signals and the instantaneous location of the spiral scanning fiber to produce a 2-D image. Specular reflections in the image are evidenced by bright spots; however by virtue of the configuration of the single, narrow beam illumination fiber and ring of collecting fibers there are relatively few spatial points meeting the specular criteria of equal angles of incidence and reflection. Hence the SFE operates without the need for crossed polarizers that reduce light collection efficiency. By utilizing this co-axial design of a single moving optical fiber with a ring of stationary collection fibers to produce 2D images, an ultrathin endoscope can be fabricated. For this study, a 1.6 mm diameter SFE probe was used. In normal "white light" imaging operation, red (635 nm), green (532 nm), and blue (442 nm) laser light are launched at the proximal end of the SFE and transmitted to the distal end using a single-mode optical fiber. However, in the present multimodal optical device, a violet (405 nm) laser replaces the red and blue illumination laser in order to obtain high resolution and high contrast surface reflection images as well as fluorescence images [43].

Since the SFE is a three channel system originally designed for RGB imaging, reflected violet light was isolated by a short wavelength dichroic beamsplitter and passed into the blue channel. The 405 nm excited autofluorescence channel consisted of light transmitted through the blue channel filter and reflected by a green dichroic beamsplitter. Finally, the 405 nm excited bacterial fluorescence is captured in the red channel [32]. Table 9 summarizes the different imaging modalities and their clinical use.
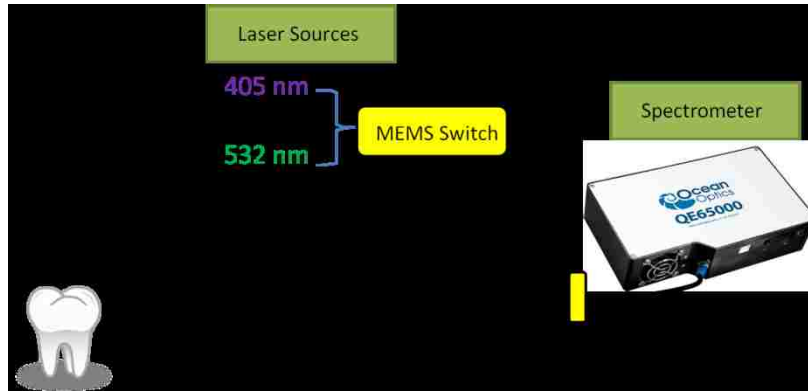
Figure 31: Schematic diagram of the dual laser spectroscopy module. A flexible fiber illuminated the teeth with either 405 nm or 532 nm laser. Switching between the lasers was controlled by a MEMS switch. The collected fluorescence was directed through an in-line filter to remove the excitation laser wavelengths before entering the spectrometer. The spectra were saved on a computer and analyzed.

6.2.3 Spectroscopy Modality

A laser-induced AF spectroscopy module was incorporated into the multimodal device and is shown in Figure 31 and the left side of Figure 30. The system uses a fiber coupled diode laser unit (FTEC2, Blue Sky Research, Milpitas, California) containing a 405-nm laser diode component (NDV4313, Nichia Corp., Tokushima, Japan), and a 532-nm fiber coupled diode laser unit (FTEC2, Blue Sky Research, Milpitas, California). Emission spectra were recorded using a commercially available miniature fiber optic spectrometer (QE65000 FL, Ocean Optics Inc., Dunedin, Florida). A 1.6-mm diameter fiber bundle was assembled in our laboratory to guide the light from the lasers to the test specimens and collect the autofluorescence. A universal serial bus (USB) connected the spectrometer to a computer for data processing.

Continuous wave output power was measured at 0.33 mW for the 405-nm laser and 0.64 mW for the 532-nm laser using an optical power meter (Model 1835-C, Newport Corp., Irvine, CA., USA). A 435 nm in-line longpass filter (GG 435, Schott North America Inc., Elmsford, NY, USA), and a 532 nm in-line notch filter (NF01-532U-25-D, Semrock, Rochester, NY, USA) were placed in series to attenuate both 405 nm and 532 nm excitation laser light at the spectrometer entrance aperture. A MEMS optical switch (Sercalo Microtechnology, Switzerland) was used to switch between 405 nm and 532 nm excitation of the tooth specimen.

6.2.4 System Integration

The prototype device was controlled using LabVIEW (National Instruments, Austin, Texas) with C language dynamic-linked libraries. Figure 32 shows the operational flow chart of the multimodal optical device. When operating in the imaging modality, the 405 nm single mode laser serves as the illumination source. Reflectance images are captured from the blue channel,

while AF images are obtained from the green channel. Lastly, bacterial fluorescence images are captured from the red channel. Since the channels operate independently from one another, the user may choose to display any combination of channels in order to obtain simultaneous multimodal images by choosing which channels are displayed in the output monitor. Images are in spatial registration since the scanning and collection optics are identical for all imaging modes. Figure 33 shows the use of the device on a patient.

AF spectra are captured at the center of the image field of view. To obtain dual laser spectroscopy the laser beam scanning fiber is temporarily halted. Then, the AF emission from 405 nm laser light is collected by the device's spectrometer. After obtaining the AF emission spectra from 405 nm excitation, the fiber optic MEMS switch selects the 532 nm laser. The AF emission spectrum from 532 nm excitation is then collected by the spectrometer. After acquiring both emission spectra, the software once again switches to the imaging mode. For a typical spectroscopic reading with 100 ms integration time per laser, approximately one second interruption between live imaging frames occurs.

Although both imaging and spectroscopy systems were validated in vitro using 1.6-mm diameter probes, the integration used separate channels for light collection, while using the same central single-mode optical fiber for illumination of imaging and spectroscopy. Two rings of 0.25-mm diameter plastic optical fibers (PJS-FB250, 0.63NA, Toray Industries, Inc) were used for these two parallel light collection channels. These fibers filled a disposable endoscope sheath of approximately 4-mm in diameter (BV-0 EndoSheath Technology, 0.6 meters in length, VisionSciences Inc). The multimode fibers surrounding the lens assembly distal to the single-mode illumination are pushed up against the clear plastic window of the sheath and held in position that does not noticeably degrade image quality.

6.2.5   Spectroscopic Analysis

AF spectra excited by 405 nm and 532 nm lasers were obtained by alternating excitation of each individual laser on each specimen in the areas with signs of early stage caries. AF from healthy enamel regions on each tooth was also recorded to obtain an intra-specimen baseline. The spectrometer integration time was set to 100 ms to reduce system noise. All emission spectra were filtered with a 13-point (corresponding to a spectral width of 4.94 nm) median filter to further remove electronic noise, followed by a 13-point Gaussian smoothing filter. Just prior to collecting emission spectra, the excitation lasers were turned off briefly, and any ambient background lighting was collected by the spectrometer with 100 ms integration time. The captured ambient spectrum was then subtracted from the fluorescence emission curves to minimize unwanted ambient light and noise from the emission spectra. This was done each time at the start of AF
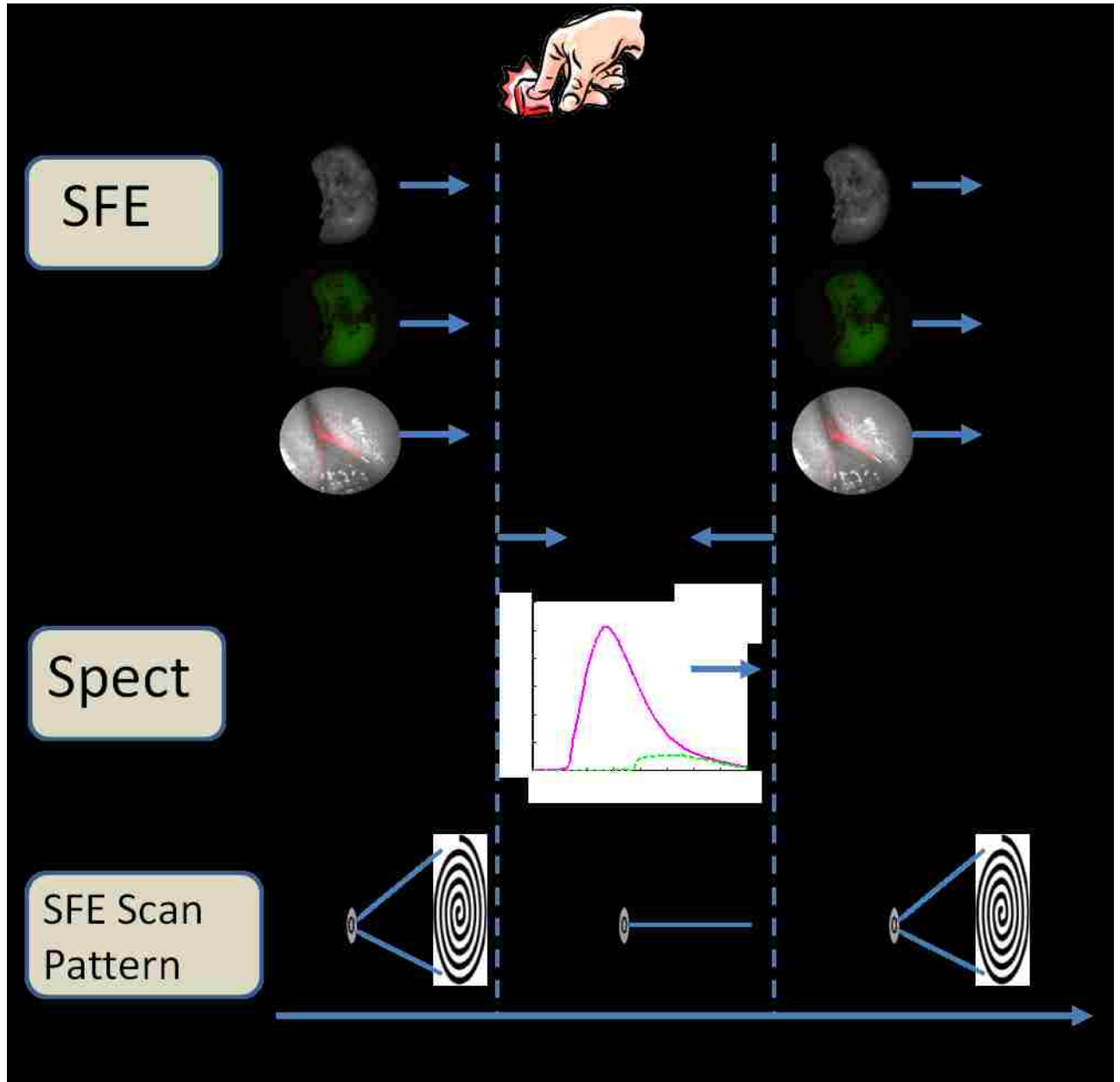
Figure 32: The operational flow of the device. The system begins in imaging mode, which captures reflectance, AF, and bacterial fluorescence images. When the clinicians notice a suspicious area, they will center the image over the area of, and push a software icon button to temporarily disable the imaging mode and begin collecting spectroscopic data. Approximately one second later, numerical spectroscopic results are displayed and the system resumes imaging.
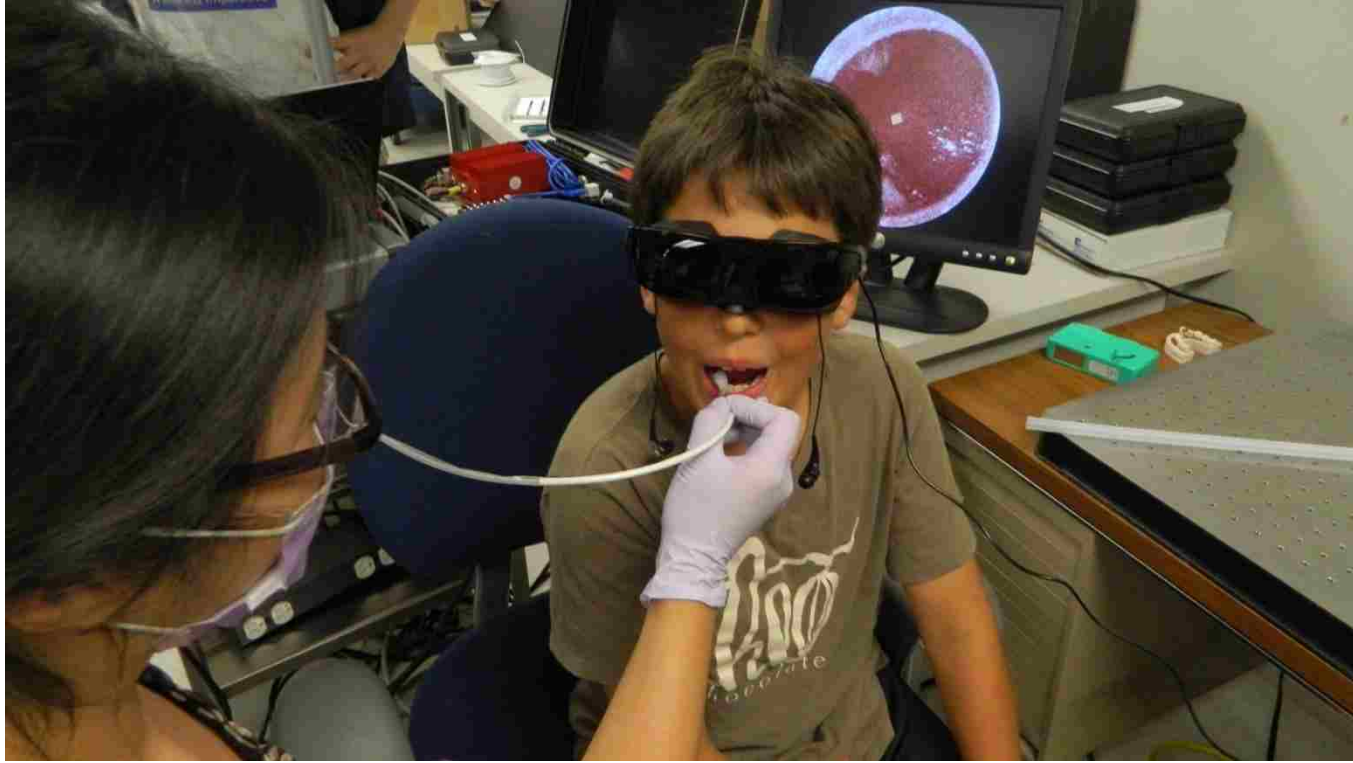
Figure 33: Use of the prototype device in vivo. The small size and flexibility of the fiber optic based probe is ideally suited for use in children. Note the display of the video image in the background. The image displayed on the screen is of the patient's tongue.

Category	Clinical Criteria
Sound	Normal texture of enamel
Caries Lesion	Opaque or slightly opaque, with loss of luster and rough, intact surface. Typically located in region of tooth with high percentage of lesion development (e.g. interproximal contact point)

Table 10: Criteria for clinical enamel classification

spectra acquisition.

The AF spectra from 405 nm and 532 nm excitation were obtained from different regions on the specimens that corresponded to different stages of enamel health. Area-under-the-curve values were obtained from the AF spectra. The area of the 405 nm spectrum was then divided by the area of the 532 nm spectrum to obtain the dual laser fluorescence ratio metric [45].

6.2.6 Test Subjects and Specimen Preparation

Extracted Specimens The institutional approved study used extracted human molars and premolars (n = 28) with sound and early stage natural caries regions. The teeth specimens were classified using the diagnostic criteria shown in Table 10. All regions with visual signs of early stage caries were noted.

The teeth were cleaned and fixed in formalin (10% neutral pH formalin, Sigma-Aldrich, St.

Figure 34: Protocol for obtaining dual laser fluorescence from a tooth. The red circle indicates a suspicious region to be measured. AF spectra are obtained at intervals of approximately 2 mm along the dashed line which spans through both sound enamel and the suspected carious lesion. The baseline reading is taken to be in a sound enamel region furthest away from the lesion and the lesion measurement is taken to be the centermost reading within the lesion area.

Louis, MO), the specimens were then stored in a 0.1% thymol (Sigma-Aldrich, St. Louis, MO) solution at room temperature.

In Vivo Patient Study   In order to examine the ability of the prototype device to function in a clinical setting, the system was tested on five patients at a pediatric dental clinic (The Center for Pediatric Dentistry, Seattle, WA, USA, Human Subjects Approval #42412). The participants were between 4 and 11 years of age, with at least one primary molar presenting an occlusal non-cavitated carious site as diagnosed according to standard of care methods. We report one case study of a 4 year old patient for detailed description here. This patient presented with an occlusal non-cavitated caries lesion, and was also scheduled for a restoration visit. Examinations began with the device operating in 405 nm reflectance mode to provide the user high-resolution and high-contrast video images of all teeth within the mouth. This served as a screening method to identify and locate the suspicious region. The device was then switched to the fluorescence imaging modality. This served to further confirm the suspicious region. If the suspicious region appeared dark compared to the background, and/or had bacterial red fluorescence signal, then it was highly likely that a caries lesion was found.

To quantitatively determine the health of the enamel, the imaging mode was temporarily interrupted so that dual laser AF spectra could be obtained. If an area of demineralization is suspected, a baseline AF spectra recorded from a healthy region of the tooth. Then, additional AF readings were sampled along in a linear fashion which passed through both sound enamel and the suspected lesion (Fig. 34). After recording the fluorescence spectra, the device resumed imaging.

6.2.7   Histology

After obtaining fluorescence spectroscopic data, 13 of the extracted specimens were selected at random for histology. Each specimen was placed in epoxy (EpoxySet, Allied high Tech Products Inc., CA). Then, 250 um thick sections were cut from the specimen using a microtome saw
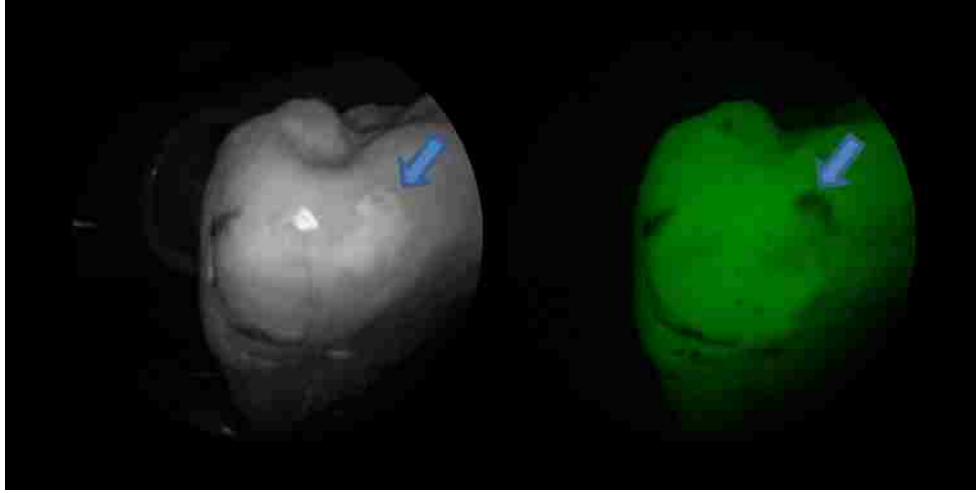
Figure 35: Images obtained from the multimodal clinical device. The left image show a 405-nm reflectance image with high resolution and contrast of the enamel surface. The right image shows the AF image of the same tooth obtained concurrently with the reflectance image. The arrows indicate a region with early caries.

(Leica SP1600, Leica Microsystems Inc., IL). The sectioned samples where then imaged with a polarized transmission microscope (Olympus BX51 optical microscope) with a quarter waveplate inserted. Lesion depth was determined from the polarized light microscope (PLM) images, and then compared to the fluorescence ratio obtained from the prototype device

6.3 Results

Figure 35 shows a set of extracted tooth images obtained from the prototype device. The left image in Figure 6 shows a 405-nm reflectance image of an extracted tooth. The right image is a concurrently obtained AF image of the same tooth.

Figure 36 shows an in vivo 405-nm image the lower front incisor at the gum line with bacterial red fluorescence overlaid. Presence of plaque is evident from the reflectance image (blue arrow) and is further supported by presence of red bacterial fluorescence.

AF spectra were obtained for all specimens using 405 nm and 532 nm excitation. Figure 37 shows typical AF emission spectra recorded from a healthy (top) and diseased (bottom) tooth specimen in vivo, which matched the expected behavior of AF described in previous studies[45, 43]. The AF spectrum from 405 nm excitation has a broad emission curve centered around 480 nm and gradually tapers off towards longer wavelengths. The 532 nm emission curve is similar in shape to the 405 nm emission curve. However, it is weaker in intensity and is shifted towards the red with the peak centered around 580 nm[43, 59, 10]. Note the increased fluorescence contribution in the 635-nm region for the diseased specimen (arrows in the right plot). This red fluorescence indicates the presence of bacterial by-products such as protoporphyrin IX. Since the 532 nm emission curve is shifted further out towards red compared
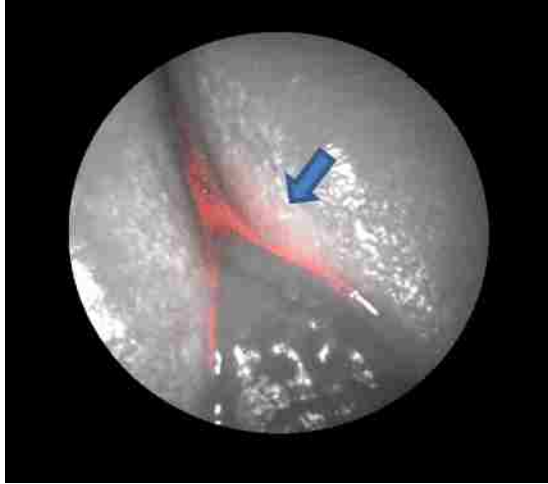
Figure 36: A mixed mode SFE image of a lower incisor viewed from the buccal facing near the gum line. The image consists of reflectance (grayscale) data with bacterial fluorescence overlaid.

to the 405 nm emission curve, and since the bacterial fluorescence is centered around 635 nm, the superposition of the 532 nm curve with the bacterial fluorescence curve leads to a very strong peak from approximately 600 to 650 nm.

Sound 405/532-nm AF ratios were obtained from a healthy region (baseline) on a tooth, as well as from a region suspected to be a carious lesion. Shown in Figure 9 is a plot that shows the obtained AF ratios from sound and demineralized enamel for each extracted specimen. Tooth-to-tooth variation in AF ratios is also seen. However, changing the metric to a ratio percent change (RPC), the variation is minimized:

$$RPC = \frac{BaselineAF - MeasuredAF}{BaselineAF}$$

In the equation, baseline AF is measured from a known sound enamel region, and measured AF is acquired from the area of interest. Using RPC, it is possible to set a threshold value that can be used to discriminate between sound and demineralized enamel. The right side of Figure 38 is the plot of RPC for sound and demineralized enamel for each extracted specimen. There was statistical significance between sound enamel and demineralized enamel using two-tailed Student's T-tests for two samples with unequal variance at a 5% significance level.

Histology via PLM confirmed presence of natural carious lesions in all 13 tested tooth specimens. Figure 39 shows a representative PLM image of a sectioned tooth with a demineralized region in the enamel at the interproximal location. The presence of an intact surface zone is visible on the surface of the enamel. A range of lesion severities from 130 um to 1200 um were measured from the PLM images. Figure 40 shows a comparison plot with lesion depth as measured from PLM for each specimen and its corresponding AF ratio change measured using the
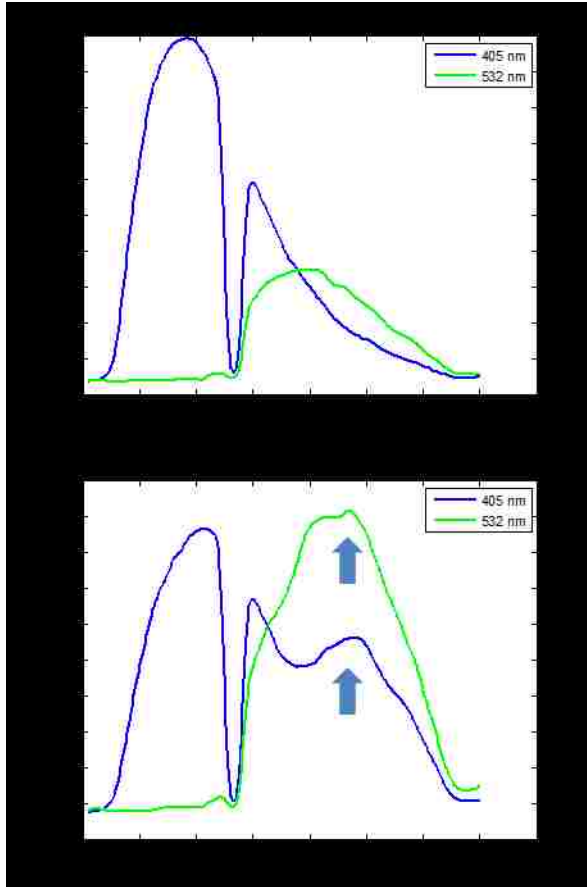
Figure 37: Typical AF emission spectra recorded from sound (top) and demineralized (bottom) enamel. The valley on the 405 nm emission curve at 532 nm is a result of the in-line 532 nm rejection filter. In the right plot, there is increased contribution from the bacterial fluorescence, which manifests as a hump-like feature centered around 635-nm in the 405 nm excited AF. The 532 nm emission curve is shifted further out towards red compared to the 405 nm emission curve. Since the bacterial fluorescence is centered around 635 nm, the superposition of the 532 nm curve with the bacterial fluorescence curve leads to stronger fluorescence from the 532 nm emission curve compared to the 405 nm emission curve from approximately 600 to 650 nm.

Figure 38: 405/532-nm AF ratios obtained from both healthy and demineralized regions for each specimen (left plot). In all case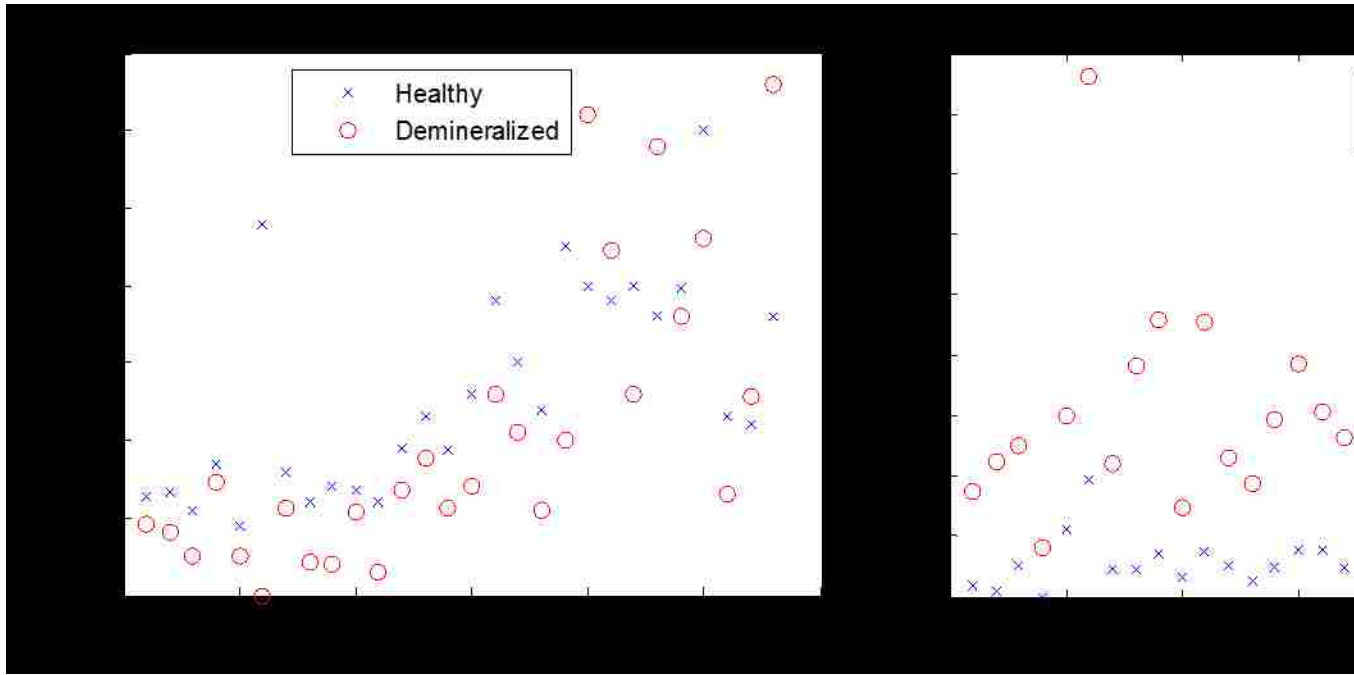s, healthy enamel exhibited higher AF ratio than demineralized ratios. However, significant inter-specimen variation is seen. When changed to RPC in AF ratio compared to a baseline AF ratio for each tooth (right plot), the delineation between healthy and demineralized enamel becomes more distinct.

dual laser fluorescence technique.

We report here a case study of a young patient (4 years of age) for the evaluation of the device's capability to work in a clinical in vivo setting. The device captured videos/images, and spectroscopic data for the patient. The small size and flexibility of the probe allowed for easy access to occlusal molar surfaces. Real time imaging and concurrent acquisition of multiple modalities allowed the device to rapidly screen for suspicious areas of tooth decay. Figure 41 shows a 405-nm reflectance image obtained with the prototype device of the young patient with a suspected occlusal caries. The lesion was located in the occlusal groove on the occlusal surface of tooth A. The lesion reflectance appears bright compared to the surrounding healthy enamel, matching the results from the ex vivo experiments as well as previous studies.7 Presence of a brown spot is observed near the center of the white spot. Dual laser spectroscopy measurements were made from the surrounding healthy enamel, white spot lesion, and brown spot lesion. A RPC value of 41% was computed for the white spot lesion, and a RPC value of 70% was computed for brown spot lesion. When interrogating both the white spot and brown spot lesion, bacterial fluorescence was evident from the characteristic hump at 635 nm.
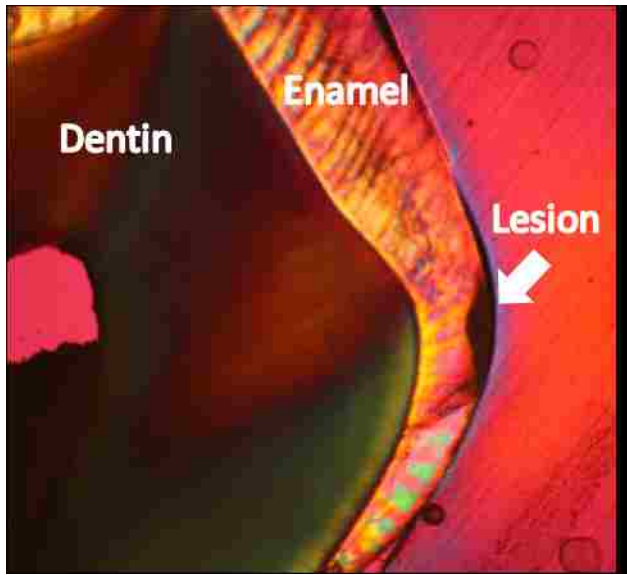
Figure 39: Polarized light microscopy used to measure depth of natural carious lesions. Shown here is an interpoximal lesion, which appears dark in the image. The depth of the lesion is 220 um.
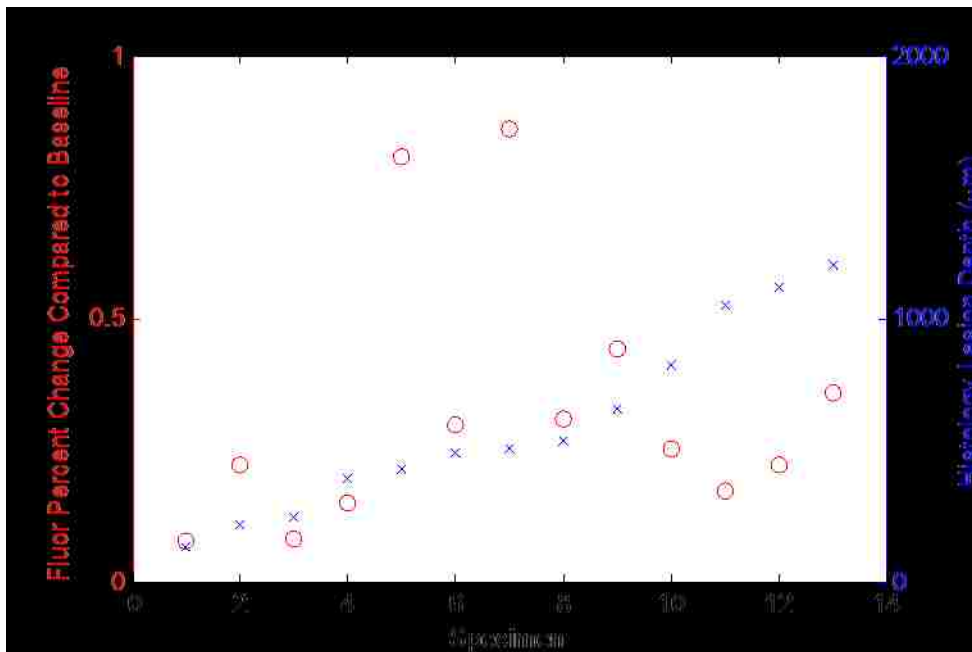
Figure 40: Comparison plot of PLM measured lesion depth in blue (axis on right) and the corresponding RPC in AF ratio in red (axis on left).
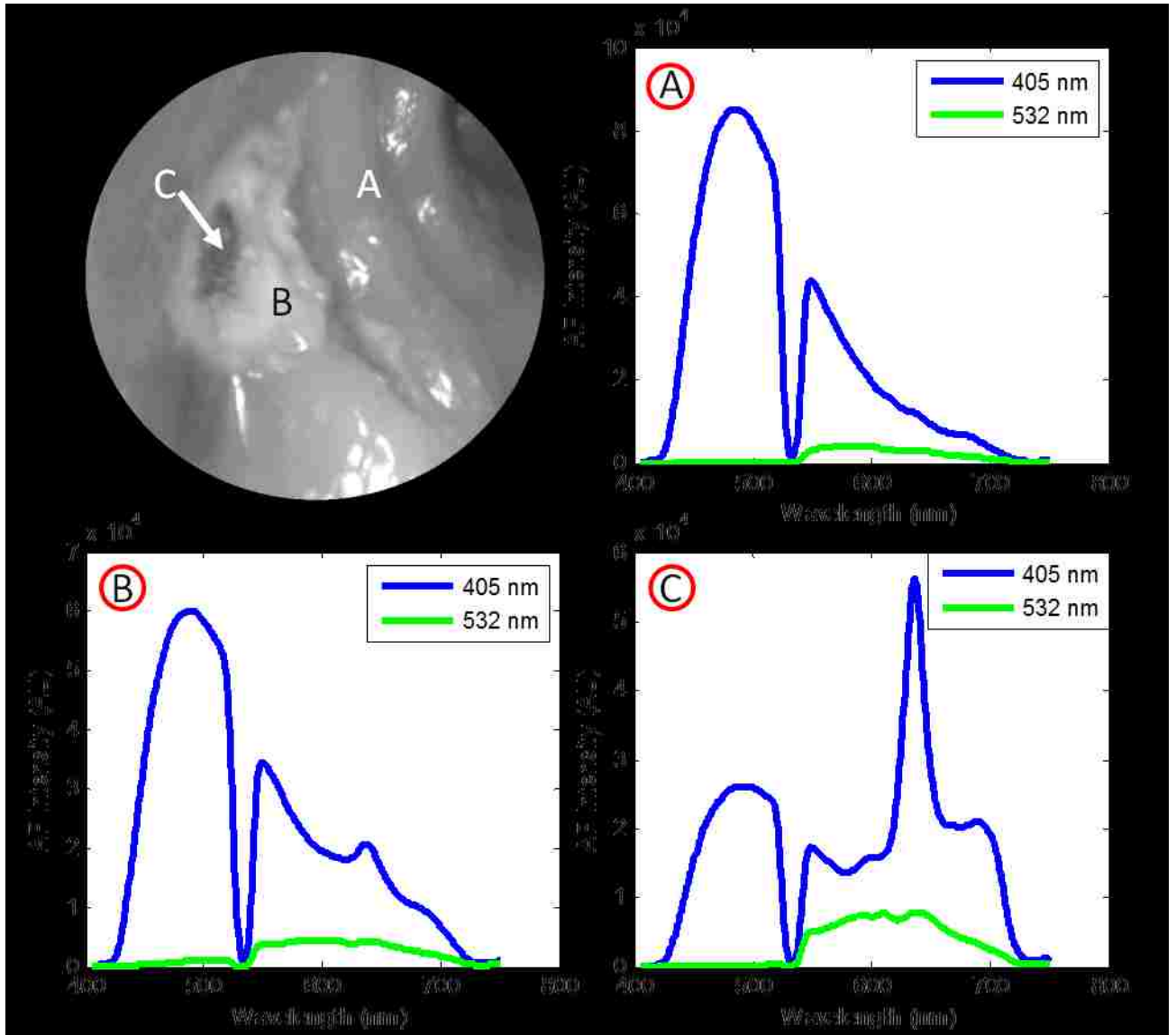
Figure 41: Top left) 405 nm reflectance images of an upper left premolar of a 4 year old patient with an occlusal lesion. The white spot lesion (B) is evident by the increased reflectance leading to a brighter appearance compared to the surrounding enamel (A). A more severe portion of the lesion (C) is evidenced by the dark spot near the center of the lesion. Top right) AF spectra from a sound region on the tooth (A). Bottom left) AF spectra from the white spot lesion (B). A RPC value of 41% is observed between sound (A) and white spot (B) enamel. Bottom right) AF spectra from the brown spot (C). A RPC value of 70% is observed between sound (A) and lesion (C). Presence of bacterial red fluorescence as evidenced by the spectral feature near 635 nm in both bottom spectra.

6.4 Discussion

The multimodal device was able to obtain high-contrast and high-resolution reflection images of teeth in vivo. The main factors that determine the clarity of the images are the penetration depth of the 405 nm illumination laser into the enamel and the scattering properties within the enamel. When compared to other visible wavelength illumination sources, the relatively shallow penetration depth of the 405 nm laser leads to reduced backscattering originating at greater depths in the enamel [44]. Backscattering from larger depths at longer wavelengths, as with conventional white light sources, is integrated and produces a composite image that often diminishes the resolution of surface details.

Fluorescence techniques have been widely investigated for dental caries [32, 10, 63, 72, 60]. However, prior techniques have either attempted to detect fluorescence from bacterial byproducts or detect the absence of fluorescence due to increases in optical scattering when enamel is demineralized [32]. The present device is capable of all previously investigated optical techniques of dental caries detection and also utilizes the new 405/532 nm AF ratio technique. Since two lasers travelling the same path are used, changes in tooth topography and distance from the enamel surface to the probe tip or angle of the enamel surface with respect to the probe tip will be mitigated by the ratiometric algorithm. Thus, fluorescence intensity effects due to tooth topography are minimized. Moreover, bacterial red fluorescence which can be detected from both the imaging as well as from the spectroscopic modes, further indicates likelihood and spatial location of caries. Additionally, the imaging capabilities of the prototype device allow for the user to quickly highlight areas for quantitative spectroscopic analysis.

Histology via PLM confirmed the presence of enamel demineralization in extracted specimens. The PLM technique involves cutting thin sections of approximately 250 um in thickness from each specimen embedded in epoxy. Thus, the measurements made from PLM are sampled in a line of finite thickness across the lesion. Additionally, since the shape of the lesion that develops is often irregular, the PLM images obtained are only samples of a particular 250 um thick section through part of the lesion. Therefore, it is possible that the obtained measurements of lesion depth are not wholly representative of the volume and severity of the entire lesion. Additional techniques such as optical coherence tomography, which is capable of obtaining three-dimensional volumetric data may be better suited at fully capturing the true severity and depths of lesions [53, 29]. However the method of polarization-sensitive optical coherent tomography (PS-OCT) could not be used adeptly by clinicians with at least 4 months experience to determine occlusal depth of demineralization more accurately than current clinical practice [71]. New sophisticated optical methods of photothermal radiometry and modulated luminescence produce depth profilometry of simulated caries [2]. Like PS-OCT, clinically imaging lesions with accurate lesion depth

measurement is an unmet challenge.

Similar to the limitation of the PLM, the dual laser AF ratio method uses a linear sampling of sound and suspected demineralized enamel. Therefore, it is possible that the obtained measurements are accurate only for the interrogated region, but may have missed the most demineralized area. Future refinements may include a protocol to scan in a two dimensional pattern with individual AF ratio measurements recorded in a frame sequential manner (15 Hz).

The dual laser AF ratio method was able to distinguish between sound and demineralized enamel with statistical significance. However, the magnitude of the percent change in AF ratio did not follow closely with the depth of lesions measured from PLM histology. One of the reasons may be the linear sampling issue described in the previous paragraphs. Also, since short wavelength light attenuates rapidly in the enamel, it is plausible that lesions of greater depth exceeded the maximum effective penetration depth of the 405 nm laser. Therefore as lesion depth severity increased, the detection sensitivity of the dual laser system decreased [44].7 Another factor which may confound the present study's results may be that since a strong portion of teeth AF is emitted from the dentin-enamel junction, thickness of the enamel and thus distance to the junction may affect the spectroscopic measurements.

Another drawback of the study is the small sample size of teeth with caries in vivo. While ex vivo experiments with extracted carious teeth yielded significant differences in AF ratios compared to sound enamel, additional studies are required to obtain more in vivo AF spectroscopic evidence of demineralized enamel. The in vivo study is ongoing and more patient data is continuously being obtained.

In conclusion, three modes of operation were conducted with the scanning fiber endoscope technology: (1) wide-field reflectance imaging, (2) wide-field autofluorescence imaging, and (3) spot laser-induced fluorescence spectroscopy. The first two optical modes were used for detection of suspicious regions of interest when screening for demineralization. The third mode was used for optical diagnosis. All modes used low power laser illumination. The prototype provided detailed images and video records of sound, demineralized, and non-cavitated lesions. The autofluorescence spectroscopic ratios were used to successfully discriminate between sound and demineralized enamel in real-time. In future prototypes, the probe diameter can be reduced in size from 4 to 1.6 millimeters without any reduction in performance by using the same light collection optical fibers and eliminating the disposable sheath by disinfecting the probe. This ultrathin, ultralight, and flexible probe could be attached to a hand tool without loss of sensitivity, such as the dental explorer. Thus, smaller dental regions, such as pits, fissures, cavities, and interproximal regions, can be more easily interrogated in a child's mouth.

7 Conclusions/Future Work

Tooth decay is a major public health problem that is steadly growing world wide, yet it has failed to receive the necessary attention to combat this epidemic. Despite advances in preventative care including toothpastes, tooth brushes, mouthrinses and other products, the prevalence of caries remains significant at the clinical and public health levels [32]. In children, many deciduous teeth are lost to early childhod caries, and the importance of these teeth cannot be neglected as loss of teeth can often lead to inability to produce dental fricatives which results in incorrect language patterns. Moreover, future permanent dentition, proper nutrition and beauty are negatively affected. All this will often lead to consequences on the psychological, social, and nutritional well-being of the child[65].

New diagnostic devices are needed to detect lesions at an early incipient stage to afford the opportunity to intervene with aggressive therapies. If found at an early stage, appropriate treatment and therapy can lead to lesion arrestment and encourage remineralization. This allows the patient to avoid the need for costly and potentially painful restorative intervention.

The standard paradigm used in medicine is to first screen for disease. After screening, a more quantatitive and specific test is performed to diagnose disease. Then, proper therapeutic options may be performed. In essence, this is a macro-to-micro approach of progressively refining the search for disease until it can be pinpointed. For example, in cardiology, ultrasound exams begins with anatomical and blood flow imaging to locate the region of interest, then followed by quantitative Doppler measurements taken at point locations to diagnose vascular disease. The developed clinical optical device follows this paradigm. By beginning examinations with 405 nm reflectance modality, the examiner can rapidly survey the mouth with high resolution and contrast to spot for suspected regions of early caries. Then, autofluorescence and bacterial fluorescence imaging can be switched on to further confirm presence of demineralization. Finally, dual laser autofluorescence is performed as a quantitative tool diagnose presence of caries.

The work of this thesis has shown that it is possible to use short wavelength 405 nm as the illumination source in order to obtain high resolution and high contrast images which show increased sensitivity in discriminating between sound and demineralized enamel. Fluorescence from teeth was investigated. It was found that florescence in teeth behave as fluorophores in a rigid solvent environment. This leads to red-edge exciation-shifts which cause emission fluorescence to be dependent on exciation wavelength, where different excitation wavelengths selectively excite different subpopulations of fluorophores. This in turn allows for two different wavelength lasers to be used to interogate different subpopulations of fluorophores in the teeth. When teeth become demineralized, the hydroxylapatite environment is changed and from which

a ratio can be computed between the two emission spectra, which can be used as a quantitative discriminator between sound and demineralized enamel.

Initial clinical testing of the clinical prototype device shows that the device is able to provide quantitative discrimination between sound and carious enamel. The high resolution reflectance imaging modality aids the user in quickly locating suspicious regions. However, further testing with more in vivo patient testing is needed. With larger sample sizes, machine-learning classifier based algortihms may be used to aid in early stage caris detection and quantification. For example, the shape of the spectroscopic curve when there is presence of bacterial porphyrin could be used as part of the classification process. Also, additional longitudinal clinical studies are currently planned and will test the efficacy of the device in monitoring therapuetic interventions on early stage caries.

References

[1] N. Hosoda A. G. Peressadko and B. N. J. Persson. Influence of surface roughness on adhesion between elastic bodies. *Phys Rev Lett*, 95:124301, 2005.

[2] Y. Finer B. T. Amaechi A. Hellen, A. Mandelis. Quantitative evaluation of the kinetics of human enamel simulated caries using photothermal radiometry and modulated luminescence. *JBO*, 16:071406, 2011.

[3] P. Anderson and J. C. Elliott. Rates of mineral loss in human enamel during in vitro demineralization perpendicular and parallel to the natural surface. *Caries Res*, 34:33–40, 2000.

[4] B. Angmar-Månsson and J.J. Ten Bosch. Optical methods for the detection and quantification of caries. *ADR*, 1(1):14–20, 1987.

[5] T. Attin. Methods for assessment of dental erosion. *Monogr Oral Sci*, 20:152–172, 2006.

[6] C. Creton B. N. J. Persson, O. Albohr and V. Peveri. Contact area between a viscoelastic solid and a hard, randomly rough, substrate. *J Chem Phys*, 120(18):8779:8793, 2004.

[7] M. E. Barbour and J. S. Rees. The laboratory assessment of enamel erosion: a review. *Jden*, 32:591–602, 2004.

[8] H.C. Benedict. Note on the fluorescence of teeth in ultra-violet rays. *Science*, 7:70–79, 1928.

[9] S. Bommer. Hautuntersuchungen im gefilterten quarzlicht. *Klin Wochenschr*, 24:1142–1144, 1927.

[10] W. Buchalla. Comparative fluorescence spectroscopy shows differences in noncavitated enamel lesions. *Caries Res*, 39:150–156, 2005.

[11] A. Lussi C. Ganss and J. Klimek. Comparison of calcium/phosphorus analysis, longitudinalmicroradiography and profilometry for the quantitative assessment of erosive demineralisation. *Caries Res*, 39:178–184, 2005.

[12] H. Kawakami-Wong J. Voronets K. Osann C. H.Wilder-Smith, P.Wilder-Smith and A. Lussi. Quantification of dental erosion in patients with gerd using optical coherence tomography before and after double-blind, randomized treatment with esomeprazole or placebo. *Am. J. Gastroenterol*, 104:2788–2795, 2009.

[13] G. D. Huynh C. L. Darling and D. Fried. Light scattering properties of natural and artificially demineralized dental enamel at 1310 nm. *JBO*, 11(3):034023, 2006.

[14] P. Ngaotheppitak C. M. Bühler and D. Fried. Imaging of occlusal dental caries (decay) with near-ir light at 1310-nm. *OSA Optics Express*, 13(2):573–582, 2005.

[15] T. D. Soper F. Helmchen C. M. Lee, C. J. Engelbrecht and E. J. Seibel. Scanning fiber endoscopy with highly flexible, 1mm catheterscopes for wide-field, full-color imaging. *J. Biophoton*, 3(5-6):385–407, 2010.

[16] I. Pretty C. Zakian and R. Ellwood. C. zakian, i. pretty, and r. ellwood. *JBO*, 14(6):064047, 2009.

[17] C. L. Darling C. Lee H. Kang D. Fried, M. Staninec and K. H. Chan. In vivo near-ir imaging of occlusal lesions at 1310-nm. *Proc of SPIE*, 7884:78840B, 2011.

[18] J. D. B. Featherstone D. Fried, R. E. Glena and W. Seka. Nature of light scattering in dental enamel and dentin at visible and near-infrared wavelengths. *Applied Optics*, 34:1278–1285, 1995.

[19] R.E. Glena B. Bordyn D. Fried, J.D.B. Featherstone and W.D. Seka. Light-scattering properties of dentin and enamel at 543, 632, and 1053 nm. *Proc Soc Photo-Opt Instrum Eng*, 1880:240–245, 1993.

[20] A.P. Demchenko. The red-edge effects: 30 years of exploration. *Luminescence*, 17:19–42, 2002.

[21] C. Höschele X. Wang B. Beyeler C. Meier E. Rakhmatullina, A. Bossen and A. Lussi. Application of the specular and diffuse reflection analysis for in vitro diagnostics of dental erosion: correlation with enamel softening, roughness, and calcium release. *Journal of Biomedical Optics*, 16(10):107002, 2011.

[22] D.R. Eyre. Cross-linking in collagen and elastin. *Ann Rev Biochem*, 53:717–748, 1984.

[23] J. P. R. Carey G. Heo D. G. Boychuk F. Orellana, A. E. Nelson and P. W. Major. Surface analysis of etched molar enamel by gas adsorption. *JDR*, 87:532–536, 2008.

[24] J.F. Freeman and M.J. Silva. Separation of the raman spectral signatures of bioapatite and collagen in compact mouse bone bleached with hydrogen peroxide. *Appl Spectrosc*, 56:770–775, 2002.

[25] D. Fujimoto. Isolation and characterization of a fluorescent material in bovine achilles tendon collagen. *Biochem Bioph Res Co*, 76:1124–1129, 1977.

[26] W.C. Galley and R.M. Purkey. Role of heterogeneity of the salvation site in electronic spectra in solution. *PNAS*, 67:1116–1121, 1970.

[27] B. K. Gandara and E. L. Truelove. Diagnosis and management of dental erosion. *J Contemp Dent Practice*, 1(1):1–17, 1999.

[28] R. C. Gonzalez and R. E. Woods. *Digital Image Processing*. Prentice Hall, 2002.

[29] C. Lee M. H. Le C. L. Darling D. L. Fried H. Kang, J. J. Jiao. Nondestructive assessment of early tooth demineralization using cross-polarization optical coherence tomography. *IEEE J. Sel Top Quantum Electron*, 16(4):870–876, 2010.

[30] M. Hannig and C. Hannig. Nanomaterials in preventative dentistry. *NNano*, 5:565–569, 2010.

[31] R.L. Hartles and A.G. Leaver. The fluorescence of teeth under ultraviolet irradiation. *Biochem J*, 54:632–638, 1953.

[32] W. Edgar I. Pretty and S. Higham. The validation of quantitative light-induced fluorescence to quantify acid erosion of human enamel. *Arch Oral Biol*, 49:285–294, 2004.

[33] J. L. Ruben J. Arends and D. Inaba. Major topics in quantitative microradiography of enamel and dentin: R parameter, mineral distribution visualization, and hyper-remineralization. *Adv. Dent. Res*, 11(4):403–414, 1997.

[34] Department of Pediatric Dentistry at the University of Washington School of Dentistry Seattle Washington personal correspondence J. H. Berg, Chair. 2011.

[35] P. C. F. Borsboom J. J. ten Bosch, H. C. van der Mei. Optical monitor of in vitro caries. *Caries Res*, 18:540–547, 1984.

[36] University of Iowa Iowa City Iowa personal correspondence J. Wefel, Professor of pediatric dentistry. 2010.

[37] L. M. Qian J. Zheng, F. Xiao and Z. R. Zhou. Erosion behavior of human tooth enamel in citric acid solution. *J Triboint*, 42:1558–1564, 2009.

[38] T. Jaeggi and A. Lussi. Prevalence, incidence and distribution of erosion. *Monogr Oral Sci*, 20:44–65, 2006.

[39] J.J. ten Bosch J.R. Zijp and R.A.J. Groenhuis. Hene-laser scattering by human enamel. *J Dent Res*, 74:1891–1898, 1995.

[40] G. Flemming K. König and R. Hibst. Laser-induced autofluorescent spectroscopy of dental caries. *Cell Mole Biol*, 44:1293–1300, 1998.

[41] T. Bonstein C. A. Orme P. J. Bush L. J. Wang, R. Tang and G. H. Nancollas. A new model for nanoscale enamel dissolution. *J Phys Chem*, 109:999–1005, 2005.

[42] T. Bonstein P. Bush L. J. Wang, R. Tang and G. H. Nancollas. Enamel demineralization in primary and permanent teeth. *J Dent Res*, 85(4):359–363, 2006.

[43] E. J. Seibel L. Zhang, L. Y. Nelson. Red-shifted fluorescence of sound dental hard tissue. *Journal of Biomedical Optics*, 16(7):071411, 2011.

[44] E. J. Seibel L. Zhang, L. Y. Nelson. Spectrally enhanced imaing of occlusal surfaces and artificial shallow enamel eerosion with a scanning fiber endoscope. *JBO*, 17(7):076019, 2012.

[45] J. H. Berg J. M. Eichenholz E. J. Seibel L. Zhang, L. Y. Nelson. Optical measure of enamel health. *IEEE GHTC*, pages 345–349, 2012.

[46] J.R. Lakowicz. *Principles of Fluorescence Spectroscopy*. Springer, New York, 2006.

[47] S.L. Jacques L.H. Wang and L.Q. Zheng. Mcml - monte carlo modeling of photon transport in multi-layered tissues. *Computer Methods and Programs in Biomedicine*, 47:131–146, 1995.

[48] G. K. Stookey M. H. van der Veen, M. Ando and E. de Josselin de Jong. A monte carlo simulation of the influence of sound enamel scattering coefficient on lesion visibility in light-induced fluorescence. *Caries Res*, 36:10–18, 2002.

[49] S. Naidoo and N. Myburgh. Nutrition, oral health and the young child. *Matern Child Nutr*, 3:312–321, 2007.

[50] U.S. Department of Health and Human Services. Preventing chronic diseases: Investing wisely in health. *National Center for Chronic Disease Prevention and Health Promotion*, 2007.

[51] P. Petersen. World health organization global policy for improvement of oral health. *Int Dent J*, 58:115–121, 2008.

[52] F. Garcia-Godoy R. Bagramian and A. Volpe. The global increase in dental caries. a pending public health crisis. *Am J Dent*, 21:3–8, 2009.

[53] J. D. B. Featherstone D. Fried R. S. Jones, C. L. Darling. Remineralization of in vitro dental caries assessed with polarization-sensitive optical coherence tomography. *JBO*, 11:014016, 2006.

[54] P.L. Fan J.G. Frazer-Dib R.H.W Brodbelt, W.J. O Brien and R. Yu. Translucency of human dental enamel. *J Dent Res*, 60:1749–1753, 1981.

[55] E.M. Rivera and M. Yamauchi. Site comparisons of dentine collagen cross-links from extracted human teeth. *Archs Oral Biol*, 38:541–546, 1993.

[56] S. L. Jacques S. A. Prahl, M. Keijzer and A. J. Welch. A monte carlo model of light propagation in tissue. *SPIE Proceedings of Dosimetry of Laser Radiation in Medicine and Biology*, 5:102–111, 1989.

[57] B. P. Joshi-A. Gaustad E. J. Seibel T. D. Wang S. J. Miller, C. M. Lee. Targeted detection of murine colonic dysplasia in vivo with flexible multi-spectral scanning fiber endoscopy. *Journal of Biomedical Optics*, 2011.

[58] D. Spitzer and J. J. ten Bosch. The absorption and scattering of light in bovine and human dental enamel. *Calcif Tiss Res*, 17:129–137, 1975.

[59] D. Spitzer and J. J. ten Bosch. Luminescence quantum yields of sound and carious dental enamel. *Calcif Tiss Res*, 24:249–251, 1977.

[60] J.L. Jayanthi J.M. Varughese A. Balan S.S. Thomas, S. Mohanty and N. Subhash. Clinical trial for detection of dental caries using laser-induced fluorescence ratio reference standard. *J Biomed Opt*, 15:27001, 2010.

[61] C. Duque R. Peres L. Rodrigues T. Parisotto, C. Steiner-Oliveira and M. Nobre dos Santos. Relationship amoung microbiological composition and presence of dental plaque, sugar exposure, social factors and different stages of early childhood caries. *Arch Oral Biol*, 55:365–373, 2010.

[62] J. J. ten Bosch. Early detection of dental caries:. In G.K. Stookey, editor, *proceedings of the 1st annual Indiana conference*, pages 81–90, Indianapolis, Indiana, US, 1996.

[63] S. Aryatawong V. Virajsilp, A. Thearmontree and D. Paiboonwarachat. Comparison of proximal caries detection in primary teeth between laser fluorescence and bitewing radiography. *Pediatr Dent*, 27:493–499, 2005.

[64] M. H. van der Veen and E. de Josselin de Jong. Application of quantitative light-induced fluorescence for assessing early caries lesions. *Monogr Oral Sc*, 17:144–162, 2000.

[65] S. Schwartz W. Low, S. Tan. The effect of severe caries on the quality of life in young children. *Ped*, 21:325–326, 1999.

[66] J. S. Wefel and J. D. Harless. Comparison of artificial white spots by microradiography and polarized light microscopy. *J Dent Res*, 63:1271–1275, 1984.

[67] J. Wu and D. Fried. High contrast near-infrared polarized reflectance images of demineralization on tooth buccal and occlusal surfaces at lambda = 1310-nm. *Lasers Surg Med*, 41(3):208–213, 2009.

[68] P.H. Warnke H. Terheyden J. Wiltfang Y. Acil, A.E. Mobasseri and I. Springer. Detection of mature collagen in human dental enamel. *Calcif Tissue Int*, 76:121–126, 2005.

[69] T. Araki Y. Fukushima and M. Yamada. Topography of fluorescence and its possible composites in human teeth. *Cell Mol Biol*, 33:725–736, 1987.

[70] X. S. Yao Z. Meng. Measurement of the refractive index of human teeth by optical coherence tomography. *Journal of Biomedical Optics*, 14(3):034010, 2009.

[71] R. S. Jones Z. Van Hilsen. Comparing potential early caries assessment methods for teledentistry. *BMC Oral Health*, 13(16):1–9, 2013.

[72] A. Zandona and D. Zero. Diagnostic tools for early caries detection. *JADA*, 137:1675–1684, 2006.